



AUBURN UNIVERSITY ENGINEERING EXPERIMENT STATION

FRACTURE ANALYSIS OF RADIAL SCIENTIFIC INSTRUMENT MODULE
REGISTRATION FITTINGS OF THE SPACE TELESCOPE

FINAL REPORT: January 15, 1985 - July 15, 1986
Contract Number: NAS8-36287
Submitted by: Auburn University
Engineering Experiment Station
Auburn University, Alabama 36849

Prepared by: C. W. Springfield, Jr.
Department of Civil Engineering
Auburn University
Auburn University, Alabama 36849

Prepared for: George C. Marshall Space Flight Center
Marshall Space Flight Center, Alabama 35812

September 10, 1986



(NASA-CR-178932) FRACTURE ANALYSIS OF
RADIAL SCIENTIFIC INSTRUMENT MODULE
REGISTRATION FITTINGS OF THE SPACE TELESCOPE
Final Report, 15 Jan. 1985 - 15 Jul. 1986
(Auburn Univ.) 81 p

N86-32773

CSCL 20K G3/39

Unclas
44663

FRACTURE ANALYSIS OF RADIAL SCIENTIFIC INSTRUMENT MODULE
REGISTRATION FITTINGS OF THE SPACE TELESCOPE

FINAL REPORT: January 15, 1985 - July 15, 1986
Contract Number: NAS8-36287
Submitted by: Auburn University
Engineering Experiment Station
Auburn University, Alabama 36849

Prepared by: C. W. Springfield, Jr.
Department of Civil Engineering
Auburn University
Auburn University, Alabama 36849

Prepared for: George C. Marshall Space Flight Center
Marshall Space Flight Center, Alabama 35812

September 10, 1986

TABLE OF CONTENTS

	<u>Page</u>
INTRODUCTION	1
REGISTRATION FITTING AT POINT A	4
REGISTRATION FITTING AT POINT B	11
REGISTRATION FITTING AT POINT C	12
REMARKS	17
TABLES	19
FIGURES	25
REFERENCES	41
APPENDIX A	42
APPENDIX B	49

INTRODUCTION

The space telescope contains various scientific instrument (SI) modules which are mounted to the Focal Plane Structure (FPS) in a statically determinate manner. This is accomplished by using three registration fittings per SI module, one resisting three translations, another resisting two and the third resisting only one. Due to thermal insulating requirements these fittings are complex devices composed of numerous pieces. The structural integrity of these fittings is of great importance to the safety of the orbiter transporting the telescope, so in addition to the stress analyses performed during the design of these components, fracture susceptibility also needs to be considered. In this work the pieces of the registration fittings for the Radial SI Module containing the Wide Field Planetary Camera were examined to determine which would endanger the orbiter if they fractured and what is the likelihood of their fracture. The latter is stated in terms of maximum allowable initial flaw sizes in these pieces.

When possible, pieces of the fittings were shown to be fail-safe through redundancy. Primarily this was done for the bolts in four bolt connections. For these it was shown that the loss of one bolt would not destroy the connection. For pieces in nonredundant configurations fatigue fracture analyses were performed.

In order to determine the maximum allowable initial flaw sizes, fatigue fracture analyses were performed using the

FLAGRO4 computer program written by T. Hu of Rockwell International [1]. This program integrates the crack growth rate per cycle equation of Collipriest [2] for a given geometry and load spectrum, beginning at a specified initial flaw size and ending when fracture instability occurs. Given the desired length of service of the parts, this program was used iteratively to determine the maximum allowable initial flaw sizes. In this work the desired length of service was taken to be four lifetimes, with a lifetime being defined as one application of the load spectrum given in Table 2.

Some of the pieces are bolts or other threaded rods. If a flaw exists at the root of a thread then there is some interaction of the two stress raising effects; i.e., the stress concentration due to the thread and the stress singularity (if Linear Elastic Fracture Mechanics methods are used) due to the flaw. The extent of this interaction is not yet well defined. In order to obtain conservative estimates of allowable initial flaw size for these pieces, a fracture analysis code called ROD, developed by C. Meyers of MSFC, which also uses the Collipriest crack growth rate equation and includes the capability of analyzing a rod with an external circumferential crack, was used by treating the thread depth as part of the flaw size. These estimates are included in this report. However, inasmuch as the possible fracture of threaded parts is a common issue in structural analysis it was decided to investigate the stress concentration/stress singularity interaction to determine appropriate methods of stress

intensity factor calculation for these geometries, and, thus, to be able to make more accurate crack growth predictions, not only for the threaded pieces of the registration fittings being analyzed here, but also for future fracture analyses of such parts. The results of this investigation are reported in Appendix B.

This project was divided into four Tasks. In Task I the identification of required fracture analyses was accomplished. In Task II the FLAGR04 code, furnished by MSFC, was implemented on Auburn University's IBM 3033 computer. In Task III stress analyses needed in addition to those used in the original design of the fittings were performed. These were needed to supply suitable input data for the fracture analyses which were performed as Task IV. This report, however, is not divided by Tasks but, instead, by fittings, these being identified by their location at points A, B or C, as indicated in Figure 1. Also shown in Figure 1 are the global coordinate directions, V_1 , V_2 and V_3 , for the structure. Forces applied in these directions are identified as A_1, A_2, A_3 at point A, B_1 at point B, etc. Table 1 shows the loads in these directions for the various events in the service of the telescope, and Table 2 shows the loading spectrum used in the fatigue fracture analyses of parts which experience complete load reversals. Some parts are loaded only during the positive or negative half of the load cycles. Some are subjected to a pretension. For these the spectrum in Table 2 was modified appropriately. The methods of analysis used and results obtained for each piece of

each fitting are reported.

REGISTRATION FITTING AT POINT A

The various pieces of the registration fitting at point A which were addressed in this work are listed in Table 3. Also shown are the materials of which each is made, the threshold stress intensity factor range, ΔK_0 , of each, and the fracture toughness, K_{IC} , of each, as well as the manner in which their fracture susceptibility was treated; i.e., a piece is listed as fail-safe or else its maximum allowable initial flaw size is specified. These are discussed as the remainder of this section.

Focal Plane Structure Side

The base (679-3973) which mounts to the FPS is shown in Figure 2. The most likely fracture scenario identified for the base was the growth of a through crack located as indicated in the figure. The loading on this crack was assumed to be due to loads applied in the V_2 direction, resisted equally by the two shear lugs. Thus, half of the load was used as a tensile stress on a central through crack model as given in Figure 3, with $w = 3.0$ inches, $t = 0.718$ inches and $\sigma_g = 0.3646 \times A_2$ ksi. This stress, σ_g , is either the stress σ_A , σ_{LO} or σ_L of Table 2 if A_2 is due to Acoustic, Lift-Off or Landing loads, respectively. From Table 1 it is found that the largest value of A_2 is 0.77 kips which is due to Lift-Off. Steps 8 and 16 of

the spectrum in Table 2 give the largest stress range, then, it being 0.56 ksi. With this applied loading a crack length equal to the plate width would not be large enough to reach the threshold stress intensity factor range of 7 ksi-inch^{0.5} for this titanium alloy. It was concluded, then, that fracture would not occur in the base.

Three flexures (679-4132) are designed to transmit force A_3 from the ball retainer to the cover. This causes the bending stress in the flexures. However, loads A_1 and A_2 , which are primarily resisted by the three radial shear slugs, cause axial forces in these flexures since the applied loads, the shear slugs and the flexures are not coplanar. This is illustrated in Figure 4, and the locations of the flexures in their V_1 - V_2 plane is also shown. For fracture the largest tensile stresses are the ones of interest, and this occurs in the flexure identified as F_b in Figure 4. It was modeled as a cantilever beam with its movable end restrained against rotation, this end being loaded transversely and axially by concentrated forces. This is shown in Figure 5. The bending stress is $\sigma_b = 19.07 \times A_3$ ksi, and the tensile stress due to axial loading is $\sigma_t = 9.53 \times A_1$ ksi. For this particular flexure the A_2 loading did not contribute to the stress. A fatigue fracture analysis was performed on the model shown in Figure 5 considering an edge crack subjected to both tension and bending using FLAGR04. In the load spectrum of Table 2, the stresses, σ_A , σ_{Lo} and σ_L , are the sum of the bending and tensile stresses. The FLAGR04 program then uses the correct

proportions of these in tension and bending. The maximum allowable initial flaw size for four lifetimes was found to be, $a_0 = 0.022$ inches.

The loads acting on the flexures are transferred to the aluminum cover (679-4135). They subject the cover alternately to tension and bending and then to compression and reversed bending, as is shown in Figure 6. The bending moment is due to the lateral force, F , and the force reacting it which is provided by the internal spacer. Their lines of action are assumed to be separated by a distance, $e = 0.903$ inches. The axial loading results from A_3 . Neither of the fatigue fracture computer programs being used has the capability to treat a cylinder subjected to both tension and bending, so a fracture model as is shown in Figure 3 was used in FLAGRO4 to represent half of the cylinder, albeit flattened into a plate. In this model $w = 2.75$ inches, which is half of the cover circumference, $t = 0.25$ inches, the cover wall thickness at the point of interest, and $\sigma_g = 1.68 \times F + 0.728 \times A_3$ ksi, with $F = 0.857 \times (A_1^2 + A_2^2)^{0.5}$ kips. It was found that for a crack half-length of over 1.3 inches no crack propagation will occur.

A bolt (679-5280) holds the aluminum cover in place. The bolt has a pretension of 8.24 kips. When A_1, A_2, A_3 are positive this bolt is subjected to an additional tension of $A_3 + 1.2 \times F$ kips, with F defined as in the preceding paragraph. When the negatives of these are applied, the bolt does not carry the A_3 load, but there is still a tensile contribution due to the $1.2 \times F$ load. As a result every cycle of loading produces two

cycles of tension in the bolt. In order to simplify the analysis in a conservative manner, it was assumed that the A_3 loading produces tensile stress in the bolt on its negative cycle also so that every cycle would experience the same maximum stress. The cross sectional area of the bolt is 0.1504 square inches, yielding a minimum stress in the bolt of 54.8 ksi and a maximum stress of $54.8 + \sigma_g$ ksi, with $\sigma_g = (A_3 + 1.2 \times F)/0.1504$ ksi, for each cycle of loading. Thus, the terms in the Maximum column of Table 2 must have the 54.8 ksi prestress added to them, all the terms in the Minimum column are simply this prestress, and in the Cycles column each number is multiplied by two. Using this load spectrum in the ROD program it was determined that fracture instability would be reached at four lifetimes for an initial circumferential flaw size of 0.069 inches. However, net section yielding will occur in this piece before fracture instability, so analyses were performed to determine what initial flaw size would produce net section yielding at four lifetimes. This flaw size was found to be 0.035 inches.

The bolt which holds the aluminum cover in place mates with an internally threaded portion of the ball lower retainer (679-4130-111). This is illustrated in Figure 7. The threaded portion experiences the same load spectrum as the bolt except that the tensile area of this piece is different. In this analysis the minimum stress was 40.6 ksi and the maximum stress was given by $40.6 + (A_3 + 1.2 \times F)/0.2029$ ksi. The ROD program used in the analysis of the bolt does not treat internally

threaded pieces, so the threaded portion of the lower retainer was treated as a plate of width, $w = 1.61$ inches, which is the circumference at its average diameter. Its plate thickness, $t = 0.126$ inches, is the difference between the outer radius of the piece (0.312 inches) and the root radius of a 7/16 inch bolt (0.186 inches). Instead of a central through crack, a through edge crack was considered, the depth of this crack being the thread depth plus an initial flaw depth, and the applied stress was assumed to be uniform. In this way it is felt that an approximation to an internal circumferential flaw was achieved. The results of this analysis predict an allowable initial flaw size of 0.011 inches.

The ball upper retainer is attached to the lower retainer by four bolts (NAS 1351) which were checked for redundancy. Figure 7 shows the retainer and the location of these bolts. In order to demonstrate the redundancy of these bolts it was assumed that one of the bolts was missing and that the other three would carry the tension and compression required to hold the fitting. The missing bolt was assumed to be the one in the fourth quadrant of the V_1 - V_2 plane, and the Lift-Off values of A_1, A_2, A_3 were used to compute the maximum tensile stress in a remaining bolt. A pretension of 2.9 kips was also applied. The maximum tensile stress in a bolt thus calculated was found to be 76.4 ksi which is less than the ultimate tensile strength of the bolt, $S_{ut} = 80$ ksi. Consequently, it was determined that three bolts are capable of carrying the load, making this connection fail-safe, and that no fracture analysis is

necessary for these.

Four bolts (NAS 1005) are used to attach the base to the FPS. These were checked for redundancy in the same manner as the ball retainer connecting bolts. The location of these bolts is shown in Figure 2. Loads A₁ and A₂ were taken to be acting in a plane located 1.25 inches above the base/FPS interface for moment calculations. The bolt assumed to be missing is the one located in the third quadrant of the V₁-V₂ plane. Again using the Lift-Off values of the applied loads and a pretension of 3.09 kips the maximum tensile stress in a bolt was found to be 102 ksi which is less than the ultimate tensile strength of 140 ksi. Thus, this connection is fail-safe, and a fracture analysis of these bolts is not required.

Scientific Instrument Side

The base on the SI side of the point A fitting (679-2152) is shown in Figure 8. A possible fracture because of a through crack located as shown in the figure was investigated. The procedure and results are quite similar to those used and discovered for the base on the FPS side; that is, the loading was half of A₂ applied to a fracture model as shown in Figure 3, but with $w = 3.24$ inches, $t = 0.88$ inches and $\sigma_g = 0.263 \times A_2$ ksi. As with the other base this stress is too small to develop a stress intensity factor range as large as the threshold value for any possible crack size.

For the jackhead (679-2230) the critical location for a

flaw is in the thread relief groove, as indicated in Figure 9. This was analyzed using the ROD program assuming a circumferential crack with a depth equal to the groove depth plus an initial crack depth. Loads A_1 and A_2 cause the same tensile stress in the jackhead during both the positive and negative halves of the loading cycles, while the A_3 load causes tensile stress during the positive half of the cycle and no stress during the negative half. As was done in the analysis of the bolt which fastens the aluminum cover, it was assumed that the tension due to A_3 loading occurs in both halves of the loading cycle so that the number of cycles in the load spectrum of Table 2 may simply be multiplied by two. This results in a crack growth rate somewhat larger than actually exists, so a conservative analysis is obtained. The cross sectional area of the jackhead is 0.1963 square inches, and a pretension of 4.84 kips is applied, so the Minimum stresses in the loading spectrum are always 24.7 ksi. The Maximum stresses in the spectrum are given by $24.7 + (A_3 + F)/0.1963$ ksi, in which $F = 0.813 \times (A_1^2 + A_2^2)^{0.5}$. The fatigue fracture analysis predicted a maximum allowable initial flaw depth of 0.084 inches to reach fracture instability at four lifetimes, but as is the case with the aluminum cover attachment bolt, net section yielding will occur prior to fracture instability. In order to reach net section yielding not before four lifetimes an initial flaw depth of 0.032 inches is maximum.

The bolts (NAS 1005) which attach the base to the SI were checked for redundancy in the manner used for the bolts

fastening the base on the FPS side of the fitting. Figure 8 shows the locations of these bolts, and the one in the third quadrant of the V_1 - V_2 plane was assumed to be missing.

Lift-Off loads were used along with a pretension of 3.07 kips. The A_1 and A_2 loads were assumed to act in a plane 1.87 inches above the base/SI interface. A maximum tensile stress in a remaining bolt was determined to be 116 ksi which is less than the ultimate strength, $S_{ut} = 140$ ksi, so this connection is also fail-safe.

REGISTRATION FITTING AT POINT B

Table 4 lists the various pieces of the registration fitting at point B which were considered in this work. The format of this table is like that of Table 3 for the fitting at point A. Except for the support plate on the SI side of the fitting, the pieces of this fitting are identical to those of the fitting at point C. Inasmuch as the loads are greater at point C, the results obtained from analyses at point C are taken as conservative results at point B. To see the details of the analyses for all the pieces of the point B fitting except the support plate the reader is referred to the section of this report titled "REGISTRATION FITTING AT POINT C". The geometry and loading of the point B support plate (679-2228) are sufficiently different from the support plate at point C that they were analyzed independently.

In order to identify likely fracture locations and to

determine the states of stress at these locations in the support plate at point B, a plane stress analysis of the support plate was performed using the SAP V finite element program [3]. The finite element model used is shown in Figure 10, along with the locations at which flaws were assumed to exist. The cut-out region in which the flexure fits was modeled by reducing the Young's modulus of the elements in that region by the ratio of the reduced thickness to the thickness of the rest of the piece. As can be seen in Figure 10, only a portion of the support plate was modeled, the remainder being treated as rigid. The most critical location found for a crack in this piece is indicated in the figure. The stress distribution at this location can be represented by that due to a combination of bending and axial loading, these being found to be given by $\sigma_b = 2.9 \times B_1$ ksi and $\sigma_t = 2.5 \times B_1$ ksi. These only occur during half of a load cycle, so the stresses in the Minimum column of Table 2 were taken to be zero. An analysis of an edge crack was performed, and it was determined that an initial crack depth of 0.153 inches is acceptable.

REGISTRATION FITTING AT POINT C

Following the format of Tables 3 and 4, Table 5 lists the pieces of the point C registration fitting which were addressed in this project along with the material, fracture toughnesses, and fracture susceptibility of each. A description of the various analyses is given in the following paragraphs.

Focal Plane Structure Side

Two possible flaw locations were investigated in the base (911-4236), these being illustrated in Figure 11 which shows two views of the base with the ball installed. At location 12 is a through crack subjected to stresses due to the C_1 loads. The fracture model is as shown in Figure 3 with $w = 4.50$ inches, $t = 0.5$ inches and $\sigma_g = 0.349 \times C_1$ ksi. As was found to be the case with the other bases, even when C_1 is due to Lift-Off this applied stress is not large enough to cause crack growth for any flaw size which can occur. The other flaw which was considered was an edge crack at location 12a. At this location the C_2 load causes both a uniform tension load and a bending load. The resulting stress is found to be $\sigma_g = 1.44 \times C_2$ ksi on the ball side of the piece, and it was assumed to decay linearly to zero on the back side. In the load spectrum of Table 2, σ_g is either σ_A , σ_{LO} or σ_L , when the applied loads are due to either Acoustic, Lift-Off or Landing sources, respectively. These stresses were divided into the appropriate tensile and bending stresses in the FLAGRO4 program in the analysis. It was found that an edge crack depth in excess of 1.5 inches would be required to develop net section yielding which will occur before fracture instability.

The stress relief groove on the stem of the ball (679-2387-110) is the most critical potential flaw location in this piece. A circumferential flaw was assumed to exist there, as is shown in Figure 12. The cyclic loading is tension due to

the force, $F = (C_1^2 + C_2^2)^{0.5}$, during both the positive and negative halves of the loading cycles. Thus the numbers in the Cycles column of Table 2 were doubled, those in the Minimum column were the prestress of 14.4 ksi and those in the Maximum column were $14.4 + F/0.3068$ ksi. It was determined that net section yielding would occur before fracture instability, at which time the flaw would have become 0.1485 inches deep. This depth is predicted to be reached at four lifetimes by a flaw of initial depth, $a_0 = 0.1475$ inches.

Four bolts (NAS 1005) fasten the base to the FPS. They were checked for redundancy in a manner similar to those of the other bases. The bolt locations are shown in Figure 11, and it was assumed that the C_1 load acts in a plane 3.14 inches above the base/FPS interface. The worst condition arises when the bolt in the fourth quadrant of the V_3-V_1 plane is missing. Assuming this bolt to be missing and a pretension of 3.09 kips, the highest remaining bolt tension was determined to be 5.88 kips, or 101 ksi. This is smaller than the ultimate tensile strength of the bolt, $S_{ut} = 140$ ksi, so this connection is fail-safe.

Scientific Instrument Side

The ball on the FPS side fits into the support plate (679-2223). As was done for the support plate in the point B fitting, a plane stress analysis was performed using the SAP V finite element program. The model used is shown in Figure 13. As is clear from the figure only a portion of the support plate

was modeled, the remainder being assumed to be rigid. The regions which are cut-out to accept the flexures were modeled by reducing the Young's modulus of the elements in these regions by the percentage that the material is actually reduced. Also shown in Figure 13 is the most critical location for the existence of an edge crack. At this cross section the stress can be represented by a contribution due to uniform axial stress and a contribution due to pure bending, $\sigma_t = 1.75 \times C_1 + 0.85 \times C_2$ ksi and $\sigma_b = 2.71 \times C_1 + 0.73 \times C_2$ ksi, respectively. Because these only occur during half of a load cycle, the minimum stresses in the applied load spectrum were taken to be zero. Net section yielding, defined in this particular analysis as the development of a plastic hinge at this cross section, is the limiting condition here. So the maximum allowable initial flaw depth for an edge crack at this location is the depth which will grow such that the cross section is reduced to a size allowing net section yielding at four lifetimes. This initial flaw depth was found to be 0.21 inches.

The support plate is connected to the base (679-2211) by three bolts. The base attaches to the SI with four bolts. This is shown in Figure 14. The possible fracture due to through cracks emanating from a bolt hole as shown in the figure was considered. Loading at this bolt was assumed to be one-third of the applied C_1 . A fracture model as is shown in Figure 15 was analyzed with $w = 2.125$ inches, $t = 0.58$ inches and the applied stress, $\sigma_g = 0.2705 \times C_1$. It was determined

that the threshold stress intensity factor range would not be reached for any possible initial crack size.

Since three bolts (NAS 1005) connect the support plate to the base rather than four, this connection was not checked for redundancy, but instead a fracture analysis was performed on the bolt subjected to the highest loading. This bolt is indicated in Figure 14. In addition to the preload of 3.07 kips, it is subjected to a fluctuating load of $0.434 \times C_1$ kips during half of a loading cycle and zero during the other half. In view of this, the minimum stresses were taken to be the prestress and the maximum stresses were the sum of the prestress and the fluctuating stress. A circumferential flaw which is 0.027 inches deep will cause net section yielding, but this flaw does not grow when subjected to the stress intensity factor range corresponding to the applied fluctuating stresses. Therefore, the maximum allowable initial circumferential flaw depth is 0.027 inches.

The four bolts (NAS 1005) which were used to attach the base to the SI were checked for redundancy. Their locations are indicated in Figure 14. The C_1 load was assumed to act in a plane 2.45 inches above the base/SI interface, and the bolt in the first quadrant of the V_3 - V_1 plane was the one assumed to be missing. The largest bolt tension due to the applied loads, which were the Lift-Off loads, was found to be 2.1 kips. This load along with the preload of 3.09 kips causes a tensile stress in the bolt of 89.5 ksi. The ultimate tensile strength of the bolt is 140 ksi, so this connection is deemed fail-safe.

REMARKS

Various pieces of the registration fittings for the Radial SI module of the Space Telescope have been examined from a fracture mechanics point of view and deemed to be fail-safe or else have had maximum allowable flaw sizes specified for them. The results of these analyses are summarized in Tables 3 - 5 and also in Appendix A which is comprised of tables in a form normally used by MSFC in summarizing fracture analysis results. In many instances the applied stress levels were so low that the threshold stress intensity factor range was never reached. In most of the others the allowable flaw sizes were large enough to be detected by visual inspection. However, for some parts, such as the flexures connecting the aluminum cover to the ball retainer in the fitting at point A, the flaw sizes were rather small. Eddy current tests are capable of detecting flaws of this size (0.022 inches x 0.1 inches), so for those which have been so tested these small flaws should represent no danger of going undetected.

In every instance approximations were made to err on the conservative side. These were pointed out in the discussions of the analyses for each fitting. One conservative approximation that was not mentioned, however, is the fact that retardation was not included in the crack propagation computations. It is probable that retardation occurs after Steps 8 and 16 in the load spectrum of Table 2, and so it is

expected that the predicted crack growth rates are larger than they are in reality resulting in smaller predicted allowable flaw sizes than actually may be tolerated.

TABLES

TABLE 1 RADIAL SI LOADS

<u>Force</u>	<u>Acoustic (kips)</u>	<u>Lift-Off (kips)</u>	<u>Landing (kips)</u>
A ₁	0.771	2.372	1.660
A ₂	0.298	0.770	0.425
A ₃	0.660	2.014	1.894
B ₁	1.213	3.459	2.091
C ₁	1.208	3.440	2.082
C ₂	0.958	2.148	0.987

TABLE 2 RADIAL SI LATCHES LOAD SPECTRUM

σ_A : Stresses Calculated Using Acoustic Loads

σ_{L0} : Stresses Calculated Using Lift-Off Loads

σ_L : Stresses Calculated Using Landing Loads

<u>Event</u>	<u>Step</u>	<u>Maximum</u>	<u>Minimum</u>	<u>Cycles</u>
Acoustics	1	$1/3 \times \sigma_A$	$1/3 \times \sigma_A$	1417
	2	$2/3 \times \sigma_A$	$2/3 \times \sigma_A$	1696
	3	σ_A	σ_A	487
Ship	4	$.39 \times \sigma_L$	$.20 \times \sigma_L$	155
	5	$.37 \times \sigma_L$	$.22 \times \sigma_L$	799
	6	$.35 \times \sigma_L$	$.24 \times \sigma_L$	13837
	7	$.33 \times \sigma_L$	$.25 \times \sigma_L$	218378
Launch	8	σ_{L0}	σ_{L0}	4
	9	$.75 \times \sigma_{L0}$	$.75 \times \sigma_{L0}$	7
	10	$.50 \times \sigma_{L0}$	$.50 \times \sigma_{L0}$	13
	11	$.25 \times \sigma_{L0}$	$.25 \times \sigma_{L0}$	30
Landing	12	σ_L	σ_L	4
	13	$.75 \times \sigma_L$	$.75 \times \sigma_L$	5
	14	$.50 \times \sigma_L$	$.50 \times \sigma_L$	10
	15	$.25 \times \sigma_L$	$.25 \times \sigma_L$	4
Launch	16	σ_{L0}	σ_{L0}	4
	17	$.75 \times \sigma_{L0}$	$.75 \times \sigma_{L0}$	7
	18	$.50 \times \sigma_{L0}$	$.50 \times \sigma_{L0}$	13
	19	$.25 \times \sigma_{L0}$	$.25 \times \sigma_{L0}$	30
Landing	20	σ_L	σ_L	4
	21	$.75 \times \sigma_L$	$.75 \times \sigma_L$	5
	22	$.50 \times \sigma_L$	$.50 \times \sigma_L$	10
	23	$.25 \times \sigma_L$	$.25 \times \sigma_L$	4

Table 3. Point A Fitting Fracture Susceptibility

Part Name	Part No.	Material	ΔK_0 (ksi $\sqrt{\text{inch}}$)	K_C (ksi $\sqrt{\text{inch}}$)	Fracture Susceptibility
FPS:					
Base	679-3973	TI 6AL-4V	6	80	NCG
Flexure	679-4132	PH13-8 Mo	7	95	TEB, $a_o = 0.022"$
Cover	679-4135	7075-T73	3.5	40	NCG
Bolt	679-5280	PH13-8 Mo	7	95	C, $a_o = 0.035"$ (NSY)
Lower Retainer	679-4130-111	TI 6AL-4V	6	80	C, $a_o = 0.011"$
Retainer Bolts	NAS 1351	Steel, $S_{UT}=80$ ksi	--	--	F-S
Base Bolts	NAS 1005	A 286	--	--	F-S
SI:					
Base	679-2152	TI 6AL-4V	6	80	NCG
Jackhead	679-2230	PH13-8 Mo	7	95	C, $a_o = 0.032"$ (NSY)
Base Bolts	NAS 1005	A 286	--	--	F-S

Key: C = Circumferential Flaw, TEB = Through Edge Beam, F-S = Fail-Safe, NCG = No Crack Growth, NSY = Net Section Yielding

Table 4. Point B Fitting Fracture Susceptibility

Part Name	Part No.	Material	ΔK_o (ksi $\sqrt{\text{inch}}$)	K_C (ksi $\sqrt{\text{inch}}$)	Fracture Susceptibility
FPS:					
Base*	911-4338	TI 6AL-4V	6	80	NCG
Ball*	679-2387-110	PH13-8 Mo	7	95	C, $a_o = 0.1475"$ (NSY)
Bolts*	NAS 1005	A 286	--	--	F-S
SI:					
Support Plate	679-2228	TI 6AL-4V	6	80	TEB, $a_o = 0.153"$
Base*	679-2211	TI 6AL-4V	6	80	NCG
Bolts* (SP/Base)	NAS 1005	A 286	15	100	C, $a_o = 0.027"$ (NSY)
Bolts* (Base/SI)	NAS 1005	A 286	--	--	F-S

Key: * - Results obtained from Point C Fitting analyses

C - Circumferential Flaw, TEB = Through Edge Beam, F-S = Fail-Safe, NCG = No Crack Growth

NSY - Net Section Yielding

Table 5. Point C Fitting Fracture Susceptibility

Part Name	Part No.	Material	ΔK_o (ksi $\sqrt{\text{inch}}$)	K_o (ksi $\sqrt{\text{inch}}$)	Fracture Susceptibility
FPS:					
Base	911-4236	TI 6AL-4V	6	80	NCG
Ball	679-2387-110	PH13-8 Mo	7	95	C, $a_o = 0.1475"$ (NSY)
Bolts	NAS 1005	A 286	--	--	F-S
SI:					
Support Plate	679-2223	TI 6AL-4V	6	80	TEB, $a_o = 0.21"$ (NSY)
Base	679-2211	TI 6AL-4V	6	80	NCG
Bolts (SP/Base)	NAS 1005	A 286	15	100	C, $a_o = 0.027"$ (NSY)
Bolts (Base/SI)	NAS 1005	A 286	--	--	F-S

Key: C = Circumferential Flaw, TEB = Through Edge Beam, F-S = Fail-Safe, NCG = No Crack Growth, NSY = Net Section Yielding

FIGURES

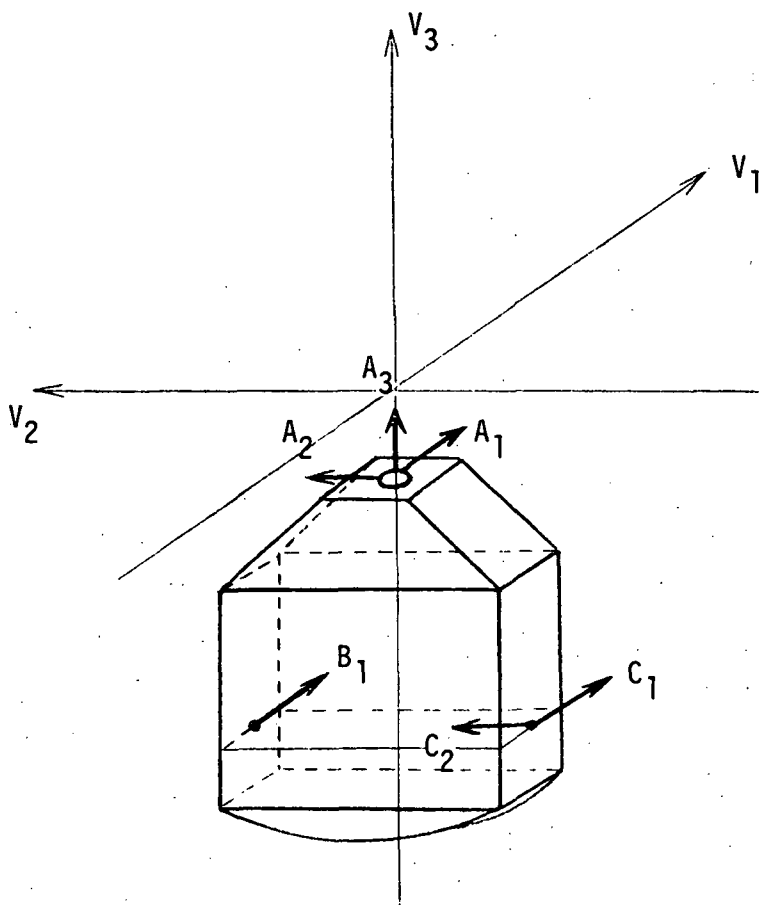


Figure 1. Radial SI in $-V_3$ Bay

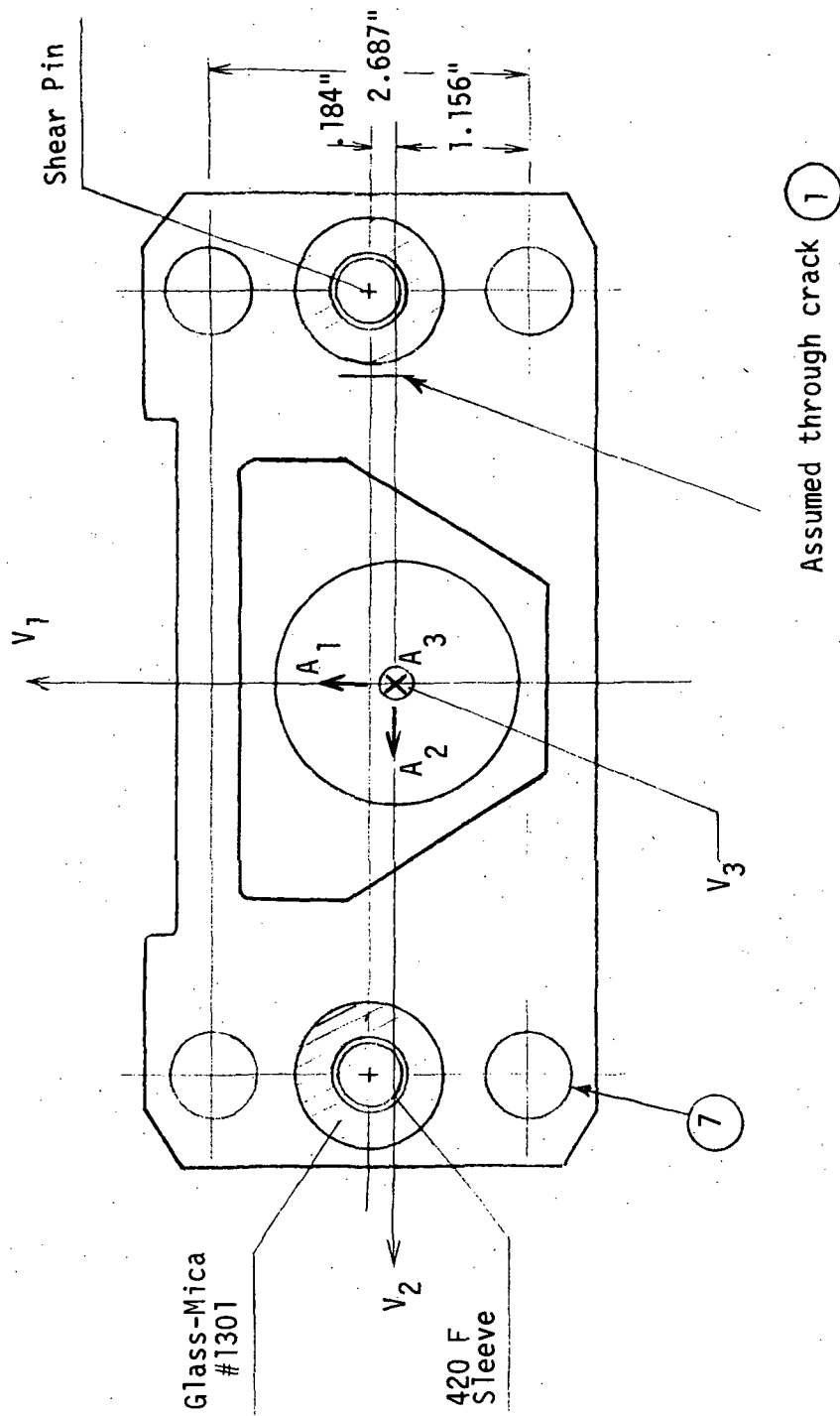
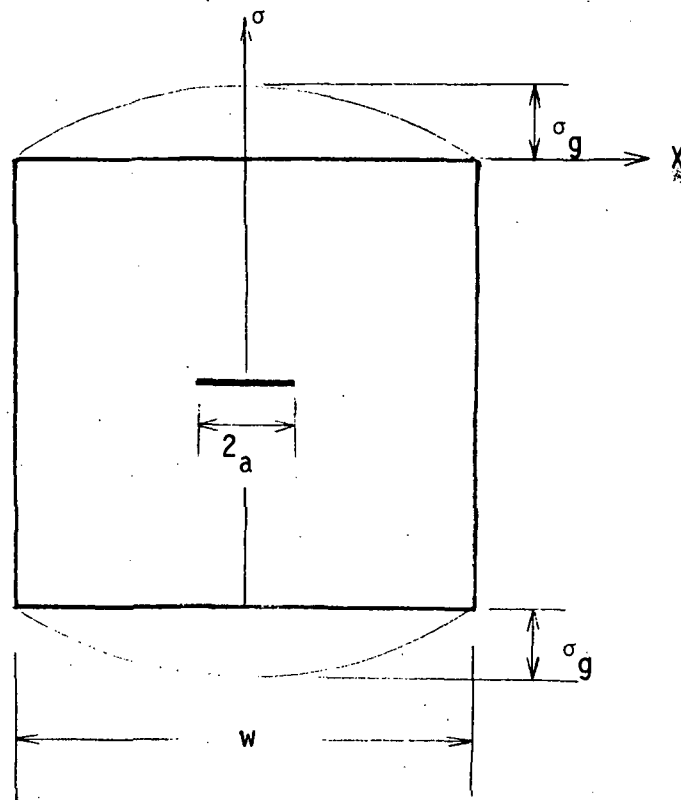


Figure 2. Base (679-3973)



$$\sigma = \sigma_g \cos \left(\frac{\pi x}{w} \right)$$

Figure 3. Central Through Crack Model

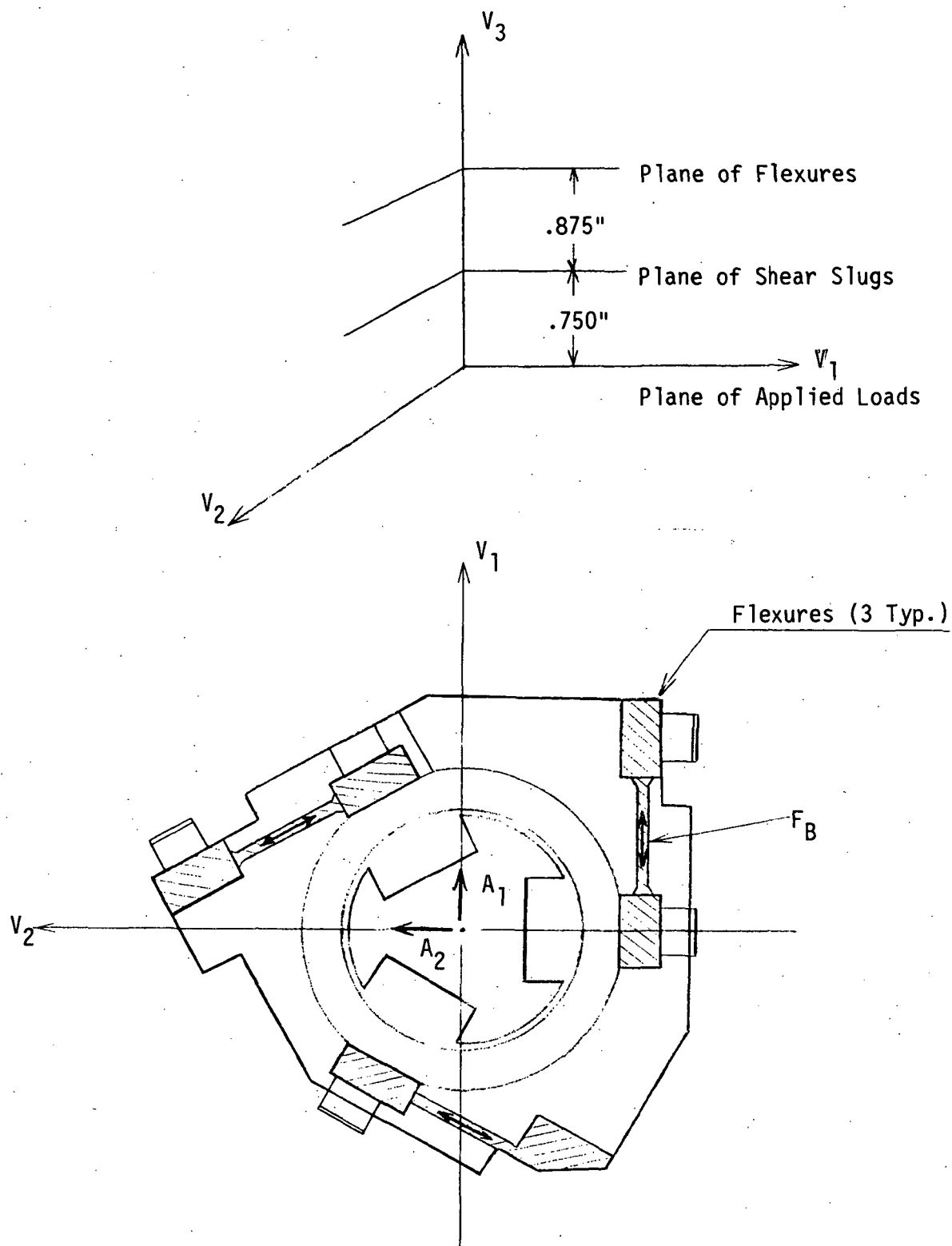


Figure 4. Locations of the Flexures and the Shear Slugs

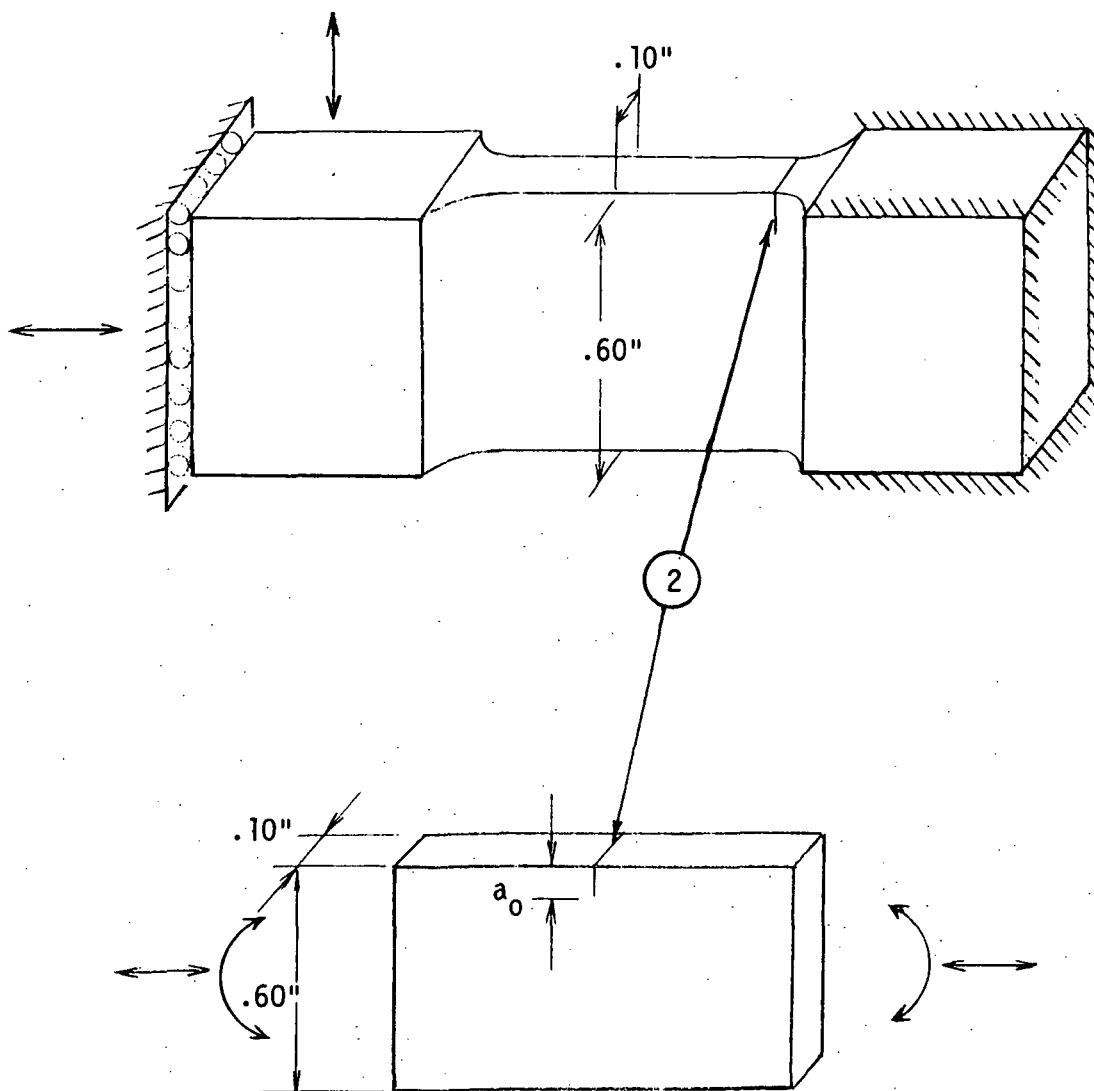


Figure 5. Flexure (679-4132) and Edge Crack Model

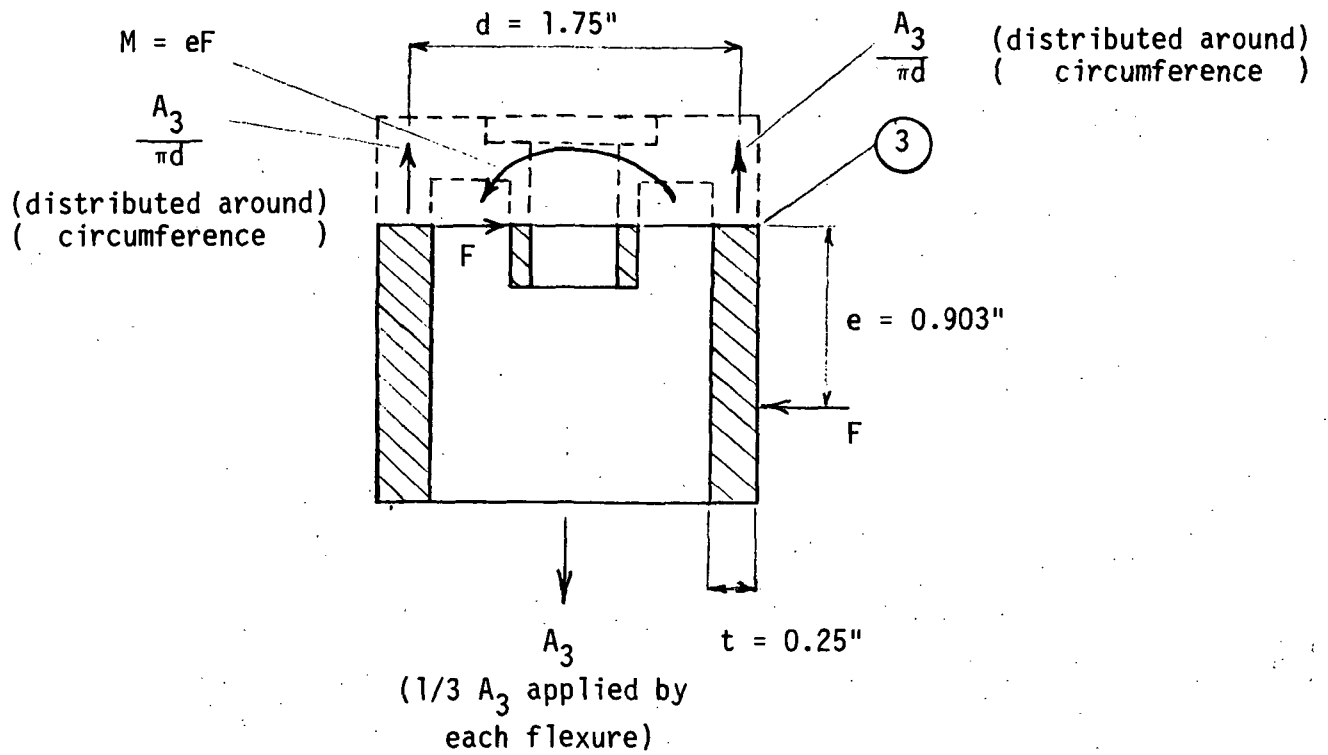


Figure 6. Section Through Aluminum Cover (679-4135)
Showing Applied Loads and Reactions

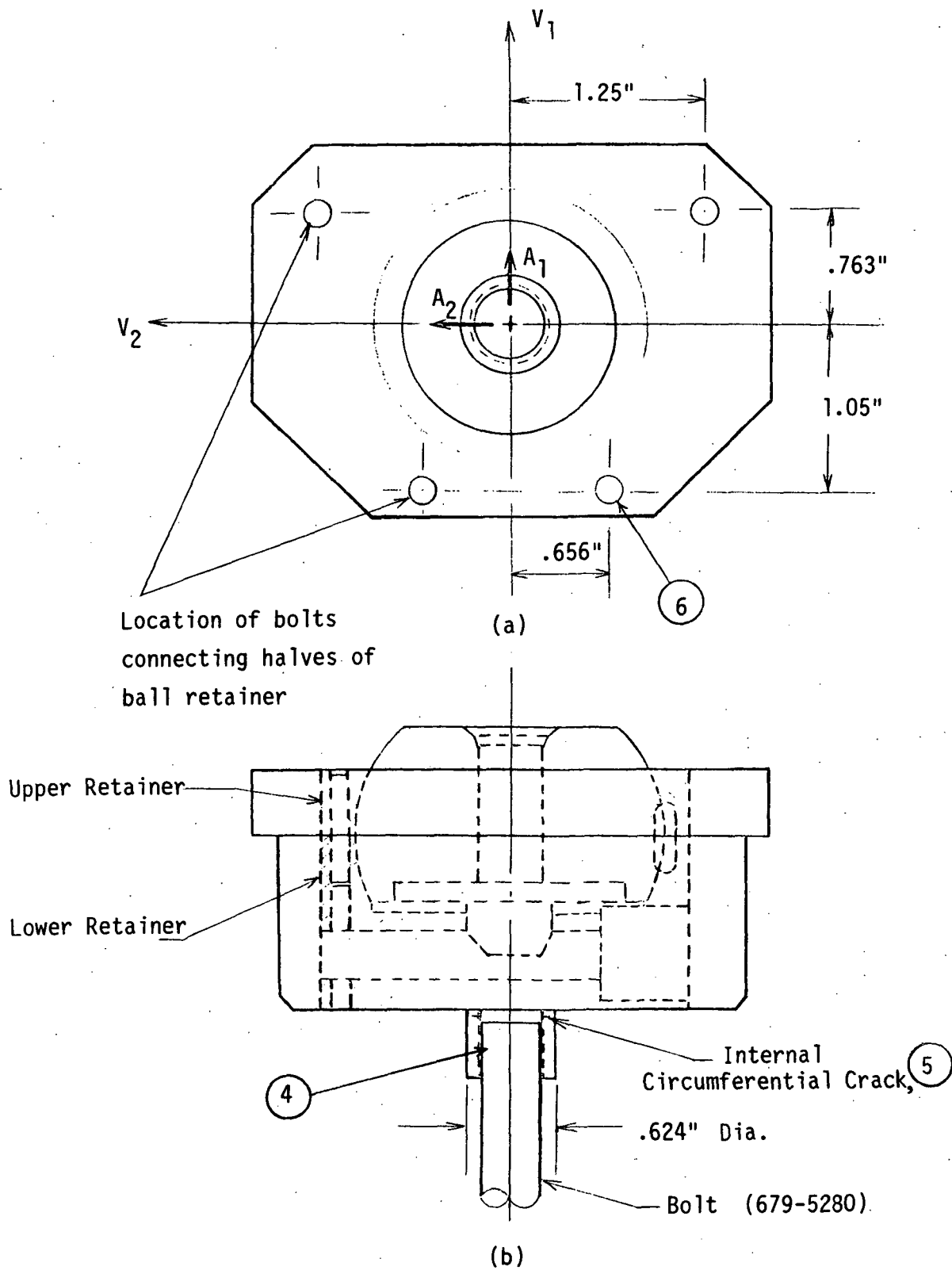


Figure 7. Ball Retainer (679-4130)

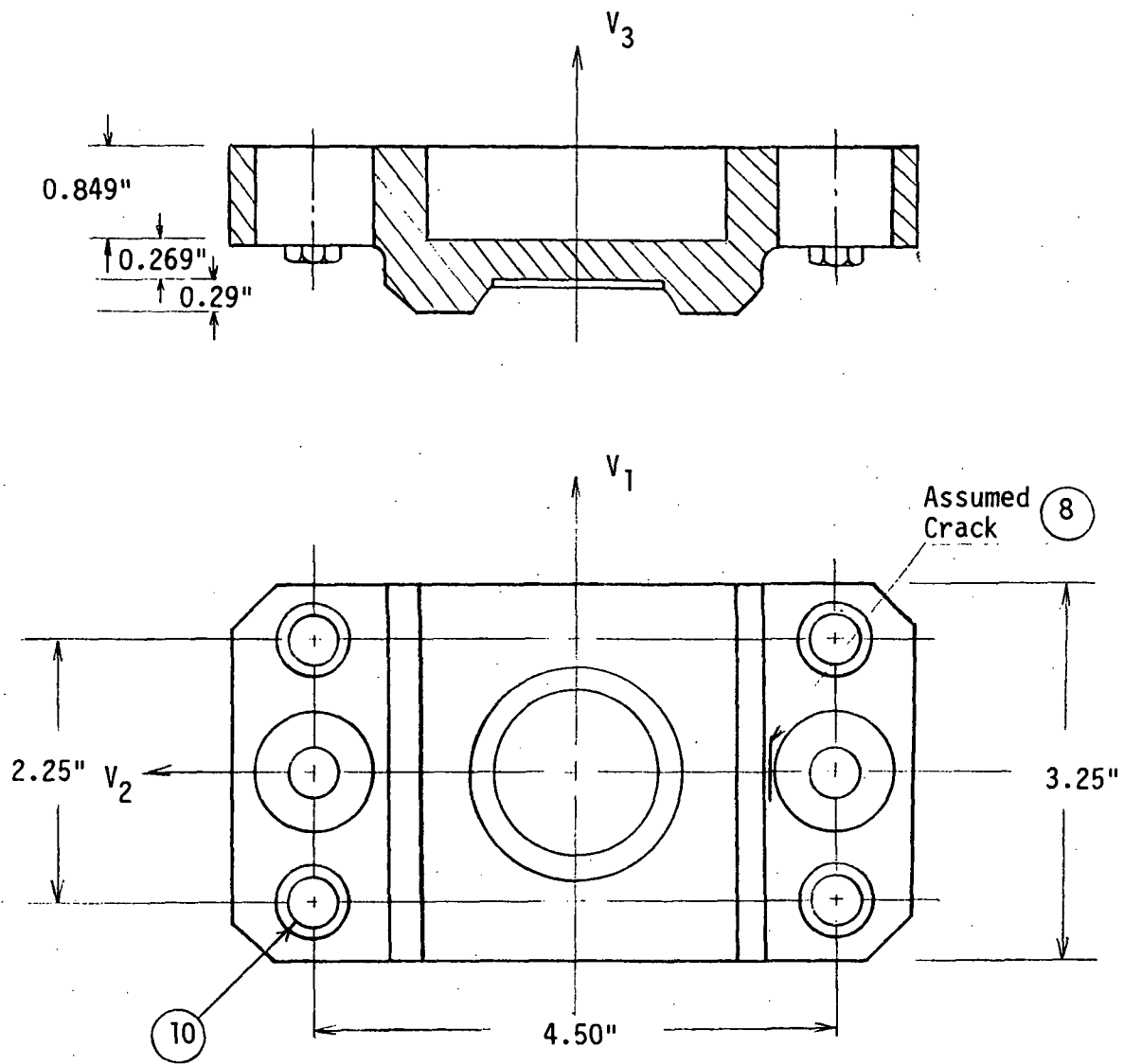


Figure 8. Point A Base, SI Side (679-2152)

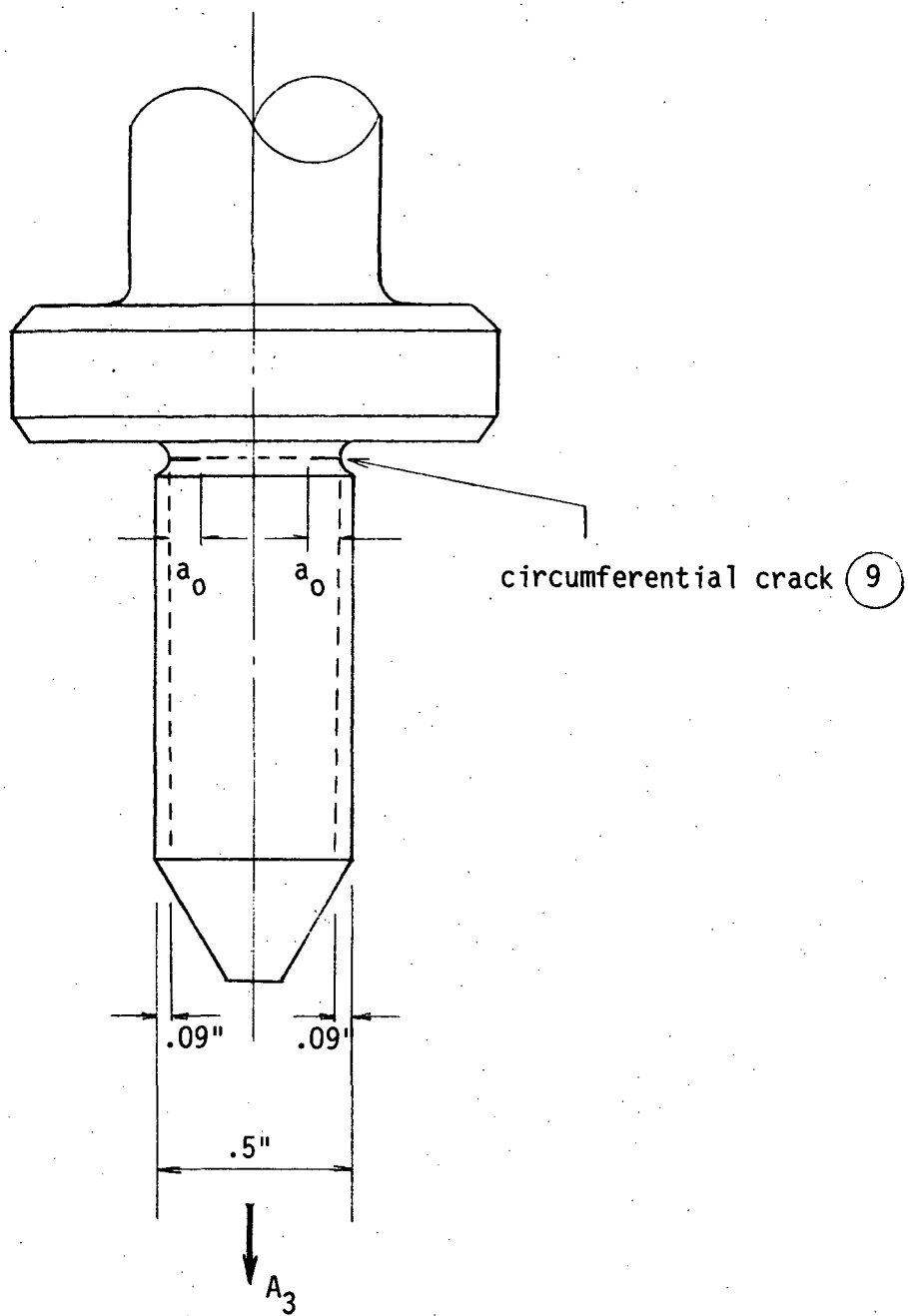


Figure 9. Jackhead

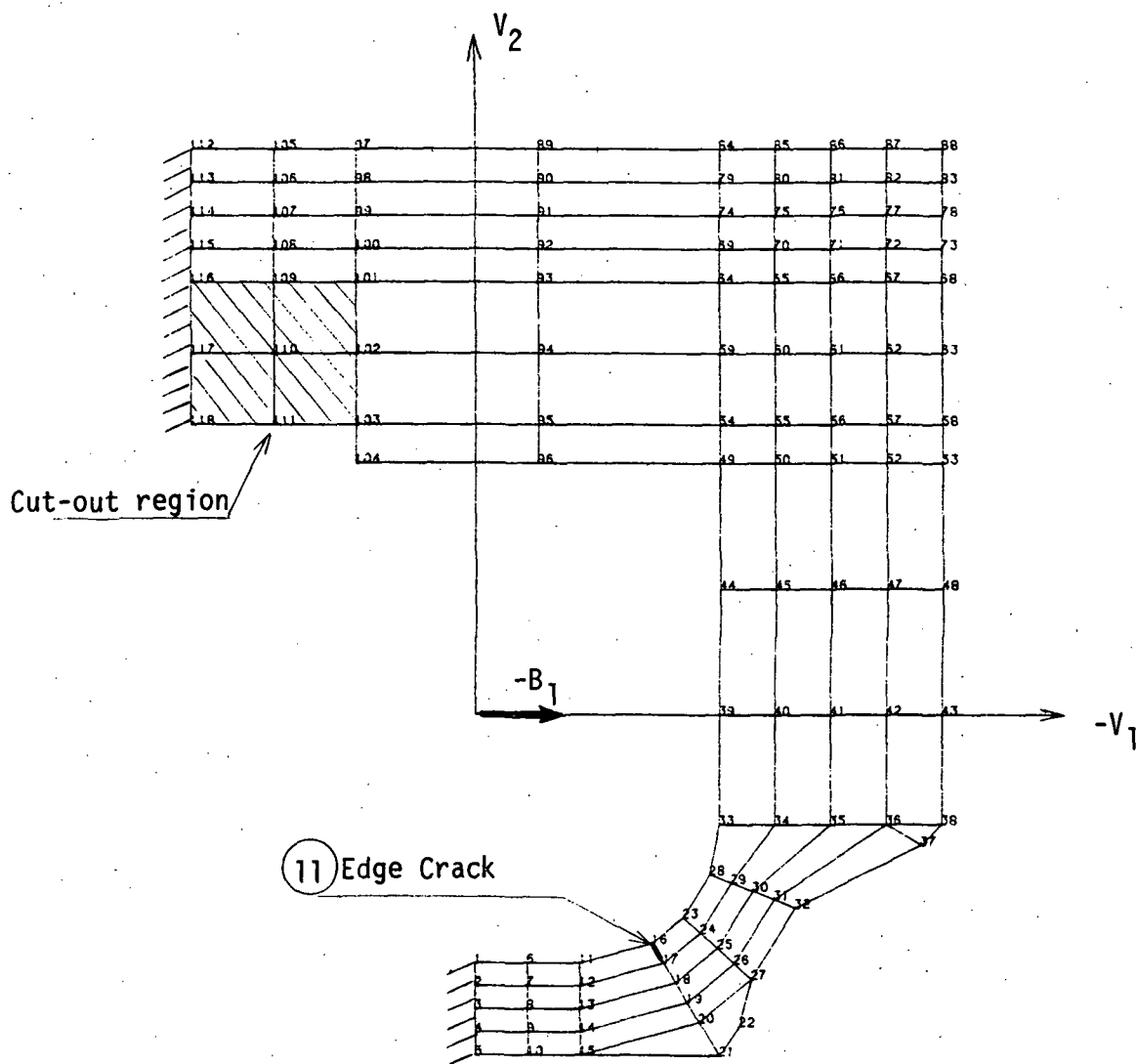


Figure 10. Finite Element Model of Point B Support Plate

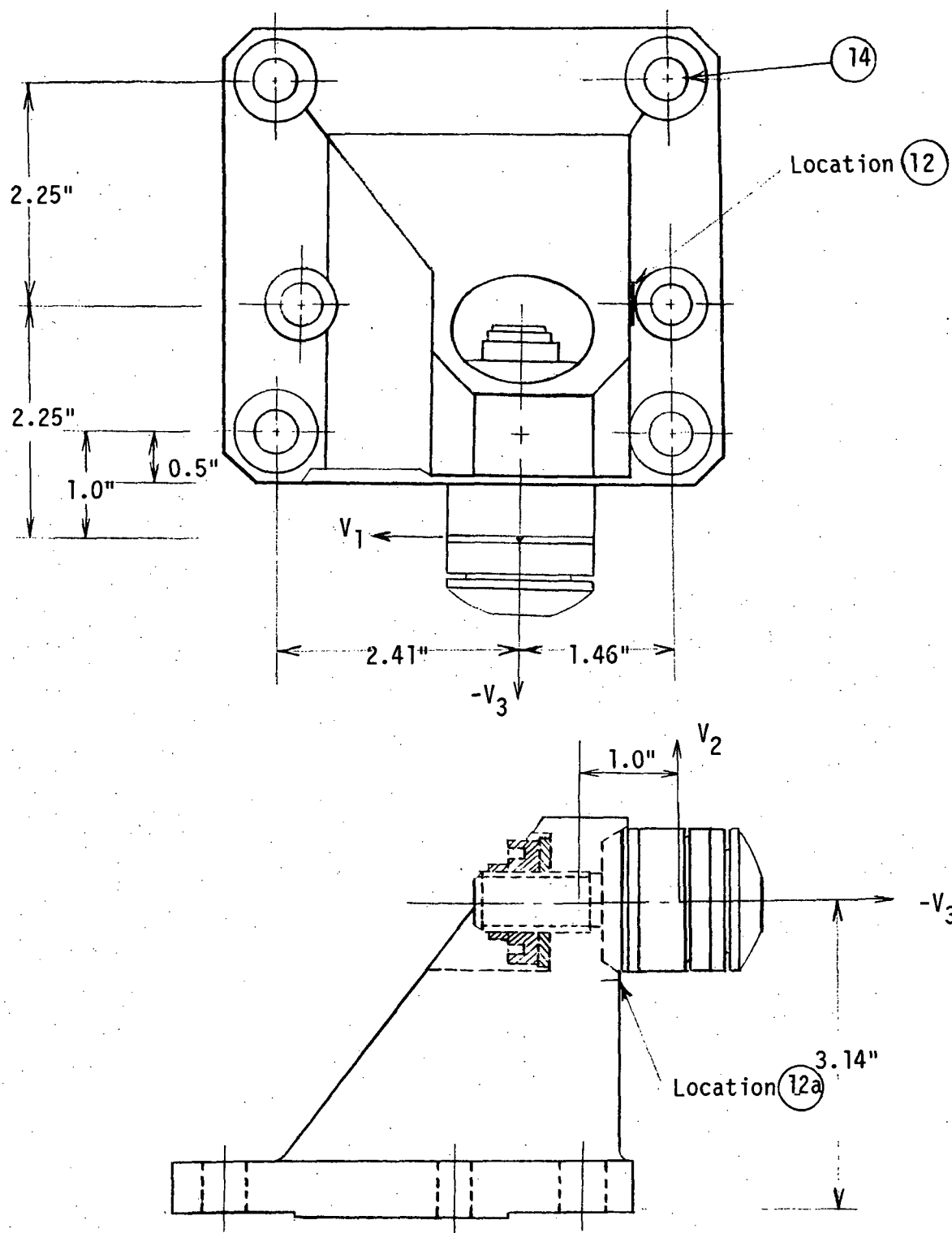


Figure 11. Point C Base, FPS Side (911-4236)

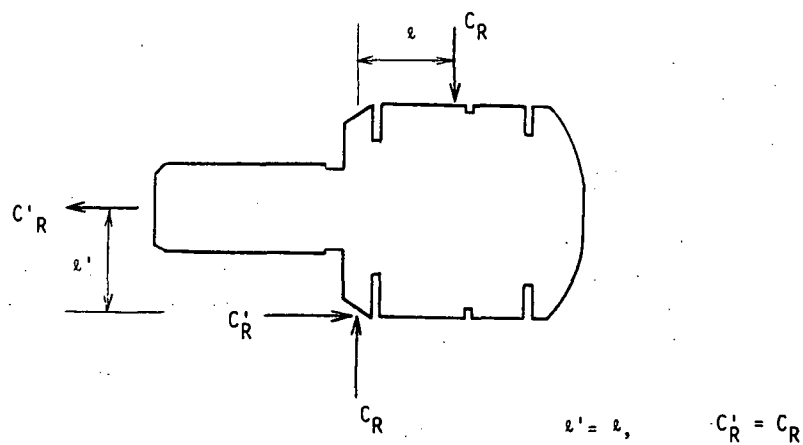
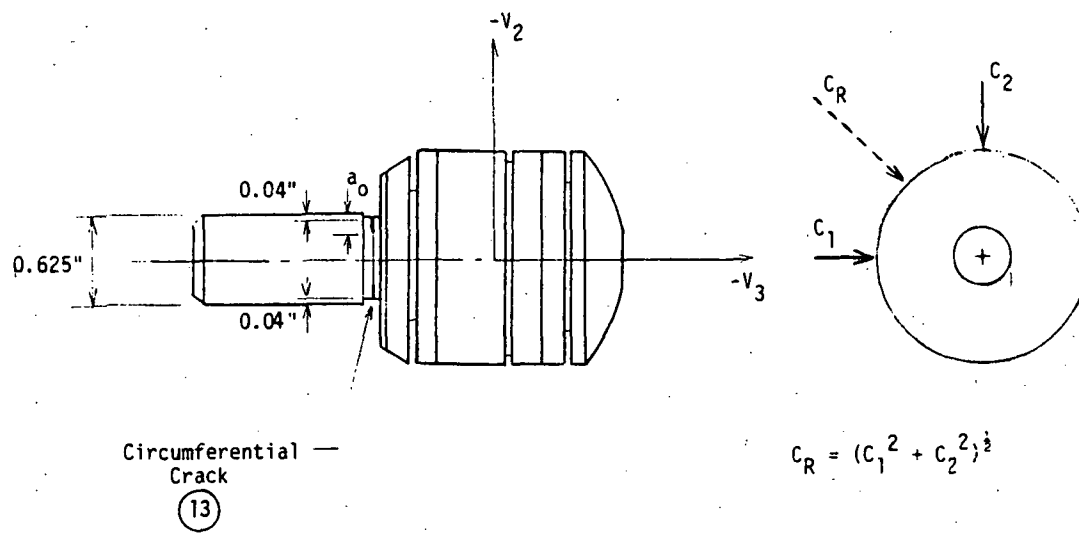


Figure 12. Circumferential Flaw of the Bolt

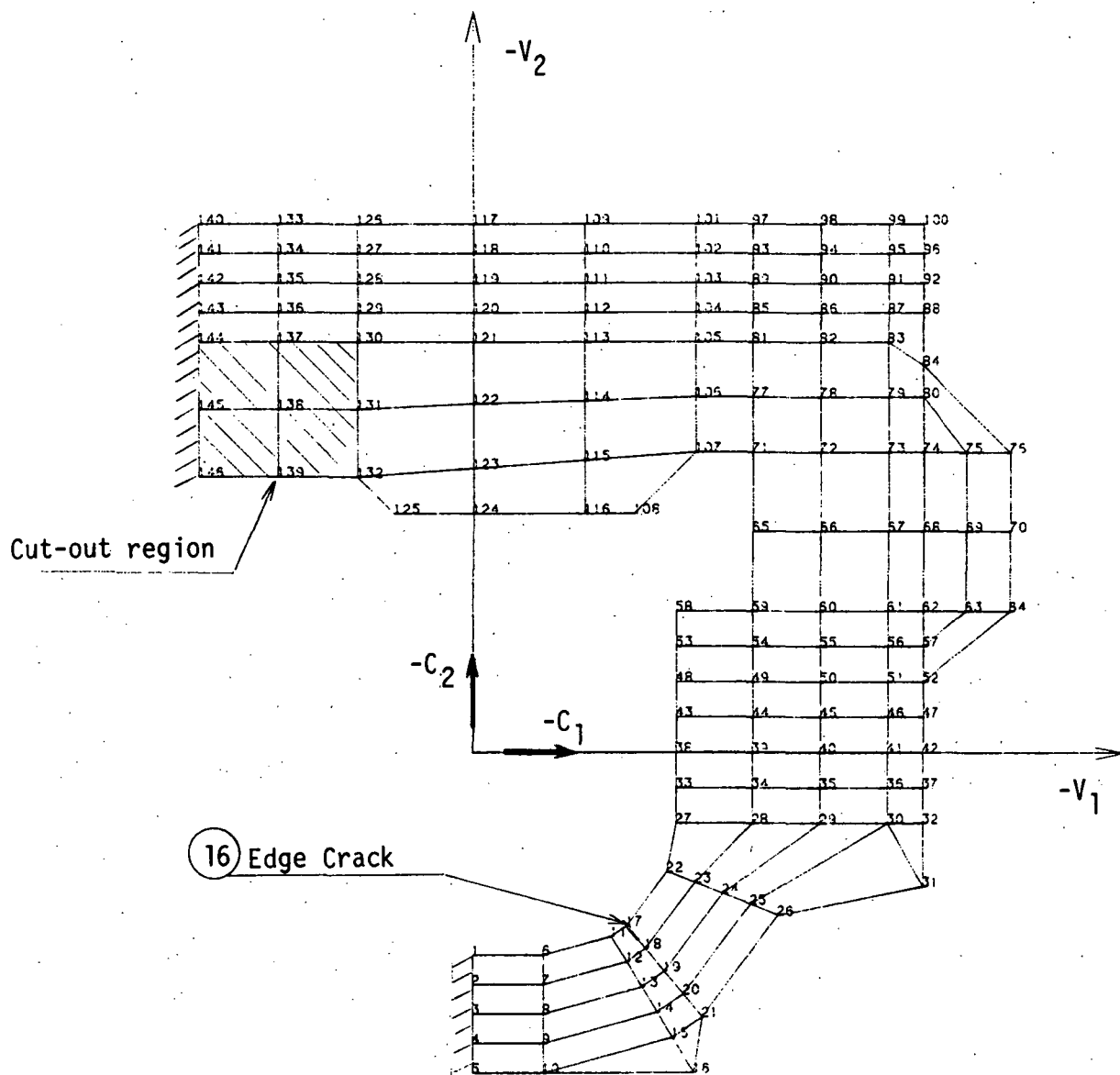


Figure 13. Finite Element Model of Point C Support Plate

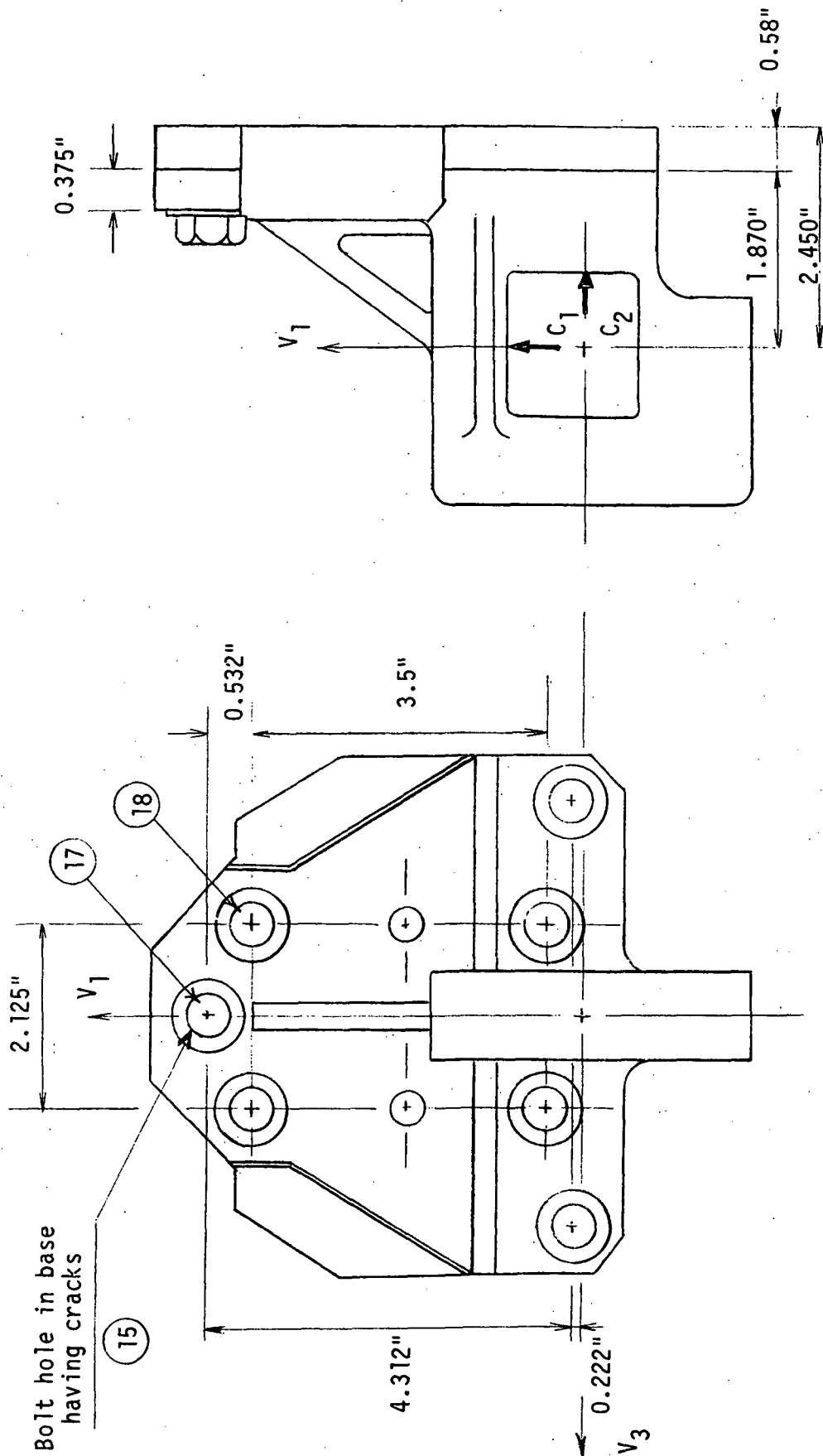
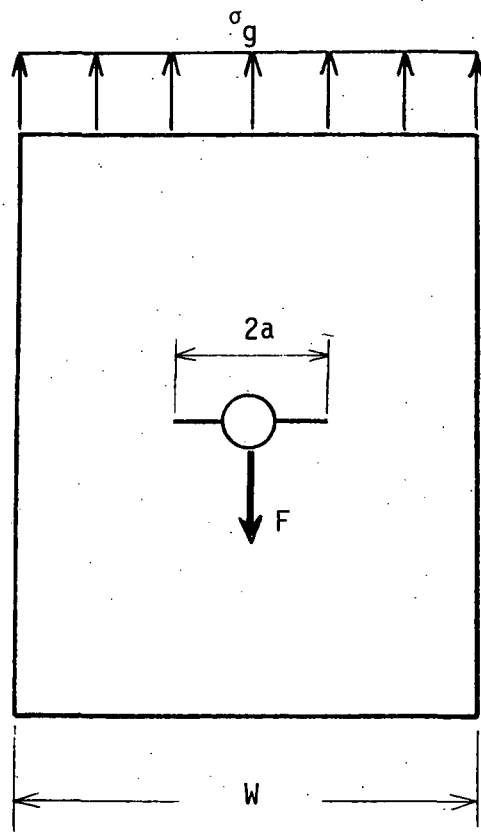


Figure 14. Point C Base (679-2211) and Support Plate (679-2223)



$$F = t \times W \times \sigma_g$$

$$K_I = \frac{\sigma_g}{2} \left[\sqrt{\pi a} + \frac{W}{\sqrt{\pi a}} \right]$$

Figure 15. Bolt Hole Crack Model

REFERENCES

1. Hu, T., Advanced Crack Propagation Predictive Analysis Computer Program "FLAGRO4", Rockwell International, September 1979.
2. Collipriest, J.E., Jr., "Experimentalists' View of the Surface Flaw Problem", Surface Crack: Physical Problems and Computational Solutions, ASME, NY, 1972, p. 43-61.
3. Anonymous, SAP V: A Structural Analysis Program for Static and Dynamic Response of Linear Systems - User's Manual, SAP Users Group, University of Southern California, October 1977.

APPENDIX A

ORGANIZATION:	MARSHALL SPACE FLIGHT CENTER		NAME:
CHART NO.:	SPACE TELESCOPE FRACTURE CONTROL		DATE:

ASSEMBLY Space Telescope

SUBASSEMBLY Radial SI, Point A, FPS Half

PART NAME	PART NUMBER	PART SIZE (IN) [*]	MATERIAL	FLAW			LIFE— TIME	STRESS (KSI)	SF
				DEPTH (IN)	LENGTH (IN)	TYPE			
Base	679-3973	t = 0.718 w = 3.0	TI-6AL-4V	0.718	>2.0	TC	4	0.3	>10 1
Flexure	679-4132	t = 0.6 w = 0.1	PH13- 8 Mo	0.022	0.1	TEB	4	61	3.3 2
Cover	679-4135	t = 0.25 w = 2.75	7075-T73	0.25	>1.3	TC	4	5.1	>10 3
Bolt	679-5280	d = 0.4375	PH13 - 8 Mo	0.035	1.374	C	4	85	2.36 4
Lower Retainer	679-4130-111	t = 0.126 w = 1.61	TI-6AL-4V	0.011	1.61	TEB	4	63	2.06 5
Retainer Bolts	NAS 1351	d = .3125	Steel, S _{ut} = 80	--	--	F-S	-	76	1.05 6
Base Bolts	NAS 1005	d = .4375	A 286	--	--	F-S	-	102	1.37 7

NOTES: *Size used in fracture mechanics model, t x w, diameter, etc.

F-S - Fail-Safe Analysis

TC - Through Center

TEB - Through Edge Beam

C - Circumferential Flaw

ORGANIZATION:		MARSHALL SPACE FLIGHT CENTER				NAME:	
CHART NO.:		SPACE TELESCOPE FRACTURE CONTROL				DATE:	
ASSEMBLY		Space Telescope					
SUBASSEMBLY		Radial SI, Point A, SI Half					

PART NAME	PART NUMBER	PART SIZE (IN) [*]	MATERIAL	FLAW			LIFE-- TIME	STRESS (KSI)	SF KEY
				DEPTH (IN)	LENGTH (IN)	TYPE			
Base	679-2152	t = 0.88 w = 3.24	TI 6AL-4V	0.88	> 2.0	TC	4	0.2	>10 8
Jackhead	679-2230	d = 0.5	PH13 - 8 Mo	0.032	1.57	C	4	45.3	4.44 9
Base Bolts	NAS 1005	d = .4375	A 286	--	--	F-S	-	116	1.21 1.0

NOTES: *Size used in fracture mechanics model, t x w, diameter, etc.

TC - Through Center Crack
C - Circumferential Flaw
F-S - Fail-Safe Analysis

ORGANIZATION:	MARSHALL SPACE FLIGHT CENTER		NAME:
CHART NO.:	SPACE TELESCOPE FRACTURE CONTROL		DATE:

ASSEMBLY Space Telescope

SUBASSEMBLY Radial SI, Point B, FPS Half

PART NAME	PART NUMBER	PART SIZE (IN) [*]	MATERIAL	FLAW			LIFE— TIME	STRESS (KSI)	SF KEY
				DEPTH (IN)	LENGTH (IN)	TYPE			
Base ⁺	911-4338	t = 0.5 w = 4.5	TI 6AL-4V	0.5	2.0	TC	4	1.2	>10
Ball ⁺	679-2387-110	d = 0.625	PH13 - 8 Mo.	.1475	1.96	C	4	27.6	7.28, 13
Bolts ⁺	NAS 1005	d = 0.4375	A 286	--	--	F-S	-	101	1.39, 14

NOTES: *Size used in fracture mechanics model, t x w, diameter, etc.

TC - Through Center Crack
C - Circumferential Flaw
F-S - Fail-Safe Analysis

⁺These results obtained from analyses of point C fitting.

ORGANIZATION:	MARSHALL SPACE FLIGHT CENTER		NAME:
CHART NO.:	SPACE TELESCOPE FRACTURE CONTROL		DATE:

ASSEMBLY		Space Telescope	
SUBASSEMBLY		Radial SI, Point B, SI Half	

PART NAME	PART NUMBER	PART SIZE (IN) [*]	MATERIAL	FLAW			LIFE— TIME	STRESS (KSI)	SF KEY
				DEPTH (IN)	LENGTH (IN)	TYPE			
Base ⁺	679-2211	t = 0.58 w = 2.125	TI 6AL-4V	0.58	>2.0	TC	4	0.9	>10 15
Support Plate	679-2228	t = 0.31 w = 1.0	TI 6AL-4V	0.153	1.0	TEB	4	18.7	6.95 11
Bolts (SP/Base) ⁺	NAS 1005	d = 0.4375	A 286	0.027	1.37	C	4	30.4	4.61 17
Bolts (Base/SI) ⁺	NAS 1005	d = 0.4375	A 286	--	--	F-S	-	89.5	1.56 18

NOTES: *Size used in fracture mechanics model, t x w, diameter, etc.

TC - Through Center Crack
TEB - Through Edge Beam
C - Circumferential Flaw

F-S - Fail-Safe Analysis

⁺These results obtained from analyses of point C fitting.

ORGANIZATION:		MARSHALL SPACE FLIGHT CENTER				NAME:			
CHART NO.:		SPACE TELESCOPE FRACTURE CONTROL				DATE:			
ASSEMBLY		Space Telescope							
SUBASSEMBLY		Radial SI, Point C, FPS Half							
PART NAME	PART NUMBER	PART SIZE (IN)*	MATERIAL	FLAW			LIFE-- TIME	STRESS (KSI)	SF KEY
				DEPTH (IN)	LENGTH (IN)	TYPE			
Base	911-4236	t = 0.5 w = 4.5	TI 6AL-4V	0.5	> 2.0	TC	4	1.2	>10 12
Ball	679-2387-110	d = 0.625	PH13 - 8 Mo.	.1475	1.96	C	4	27.6	7.28 13
Bolts	NAS 1005	d = 0.4375	A286	--	--	F-S	-	101	1.39 14
NOTES: *Size used in fracture mechanics model, t x w, diameter, etc. TC - Through Center Crack C - Circumferential Flaw F-S - Fail-Safe Analysis									

ORGANIZATION:		MARSHALL SPACE FLIGHT CENTER				NAME:			
CHART NO.:		SPACE TELESCOPE FRACTURE CONTROL				DATE:			
<div style="display: flex; justify-content: space-between; padding: 10px;"> <div style="width: 45%;"> <p>ASSEMBLY <u>Space Telescope</u></p> <p>SUBASSEMBLY <u>Radial SI, Point C, SI Half</u></p> </div> </div>									
PART NAME	PART NUMBER	PART SIZE (IN)*	MATERIAL	FLAW			LIFE-- TIME	STRESS (KSI)	SF KEY
				DEPTH (IN)	LENGTH (IN)	TYPE			
Base	679-2211	t = 0.58 w = 2.125	TI 6AL-4V	0.58	>2.0	TC	4	0.9	>10 15
Support Plate	679-2223	t = 0.42 w = 1.0	TI 6AL-4V	0.21	1.0	TEB	4	18.7	6.95 16
Bolts (SP/Base)	NAS 1005	d = .4375	A 286	0.027	1.37	C	4	30.4	4.61 17
Bolts (Base/SI)	NAS 1005	d = .4375	A 286	--	--	F-S	-	89.5	1.56 18
<p>NOTES: *Size used in fracture mechanics model, t x w, diameter, etc.</p> <div style="display: flex; justify-content: space-between;"> <div> <p>TC - Through Center</p> <p>TEB- Through Edge Beam</p> <p>C - Circumferential Flaw</p> </div> <div> <p>F-S - Fail-Safe Analysis</p> </div> </div>									

APPENDIX B - INVESTIGATION OF STRESS CONCENTRATION FACTOR -
STRESS INTENSITY FACTOR INTERACTION FOR FLAWS IN FILLETED RODS

During the course of this project several filleted rods and threaded fasteners were analyzed to establish a maximum allowable flaw size at the fillet or thread root for each. Insufficient work has been reported for stress intensity factor (SIF) solutions of these geometries to allow fatigue fracture analysis methods to be developed. Recently, Nord has used finite elements to analyze some threaded rod geometries [B-1], and he is currently incorporating his results in the Del-West fatigue fracture program for use by MSFC. Since there is very little data with which to compare his results, his results cannot be verified at this time. For the analyses of threaded and filleted rods in this work approximate means for determining the SIF were used. There were two approaches which were considered. One was to determine the stress concentration factor for the fillet and increase the applied stress in the fatigue fracture analysis by this factor. The fatigue fracture analysis was to be performed for a nonfilleted bar with an initially circular surface flaw. It was thought that this would lead to conservative results; i.e., prediction of crack growth more rapid than actually would occur. The other approach was to assume that in the fillet there was a circumferential surface flaw extending around the entire circumference. By treating the fillet depth as part of the flaw size a fatigue fracture analysis could be performed since there are solutions available for this problem. Again, it was felt that this would yield conservative results. The results reported for such pieces in this document were obtained in this latter manner.

Since a lack of SIF solutions for surface flaws occurring in fillets prevents accurate estimates of growth for these flaws, it was decided to investigate these flaw geometries using finite element techniques. Analyses of rods having circular surface flaws were analyzed to determine the interaction of the stress concentration factors of the fillets with the stress intensity factor distributions of the flaws. Figure B-1 shows the generic filleted rod geometry which was analyzed. For all the rods considered the difference between the large diameter and the small diameter was twice the fillet radius. All dimensions were normalized by the small diameter. Thus, there were two dimensionless parameters which characterized the rod geometry; r/d , and a/d . The lengths of the rods were long enough to not affect the results. Typical elastic constant for steel ($E = 30,000,000$ psi, $\nu = 0.3$) were used.

Stress intensity factor distributions around the crack fronts for the various geometries were determined from three-dimensional finite element analyses. By assuming two surface flaws in the bars located 180° apart the various symmetries allowed a model of one eighth of a rod to be used. The sizes of the flaws considered were small enough that no interaction between the flaws should have occurred, so it is considered that the results of only one flaw in a rod would be essentially the same. A typical finite element mesh used is shown in Figure B-2. The region surrounding the crack front was modeled with collapsed sided, 20 noded, isoparametric elements with the mid-edge nodes of the radial edges moved to the quarter point to produce the proper strain singularity at the crack front. This modeling technique was suggested by Barsoum [B-2]. Inasmuch as this is a displacement based

finite element method, the SIF must be determined by post-processing the displacements in some way. The SIF were determined from these results in two ways; by using the nodal displacements in the analytical expressions for displacement, and by using an energy release rate method developed by deLorenzi [B-3, B-4]. Each of these methods is discussed in the following paragraphs.

The displacement functions in the finite elements are assumed in terms of their values at their nodes, which are the displacement values determined in the finite element solution. When the modeling technique of Barsoum is used the displacement function along a radial line originating at the crack front is given by

$$u = u_1 + [4u_2 - u_3 - 3u_1] \sqrt{\frac{r}{L}} + [2u_3 + 2u_1 - 4u_2] \frac{r}{L}$$

In this, u_1 is the displacement at the crack front node, u_2 is the displacement at the quarter point node, and u_3 is the displacement at the corner node away from the crack front. On the other hand the expression for displacement in the vicinity of a crack is known to be of the form,

$$u = \frac{K_I}{2G} \sqrt{\frac{r}{2\pi}} \quad (C-1)$$

The parameter, C , depends on the proximity to the free surface along the crack front. Equating the coefficients of the r terms in the above equations yields:

$$K_I = \frac{2G}{C-1} \sqrt{\frac{2\pi}{L}} [4u_2 - u_3 - 3u_1]$$

Thus, one way to determine the SIF is to utilize the displacements determined by the finite element solution in this equation. This method is sometimes referred to as the "displacement substitution method" and will be in this report.

Since the stress intensity factor is related to the amount of energy released when a crack grows an incremental amount, calculating the energy release rate for a crack provides a reliable means of determining SIF. Several schemes for calculating the energy release rate for flaws have been reported over the years. Most of these, in one way or another, calculate the difference in strain energy of two bodies identical in every way except that the crack size of one is slightly larger than that of the other. Dividing this difference in strain energy by the difference in the crack sizes yields an approximation of the energy release rate. In the limit, as the difference in crack sizes approaches zero, this approximation approaches the exact energy release rate. Thus, the accuracy of the calculation depends on the increment in crack size used. Recently, utilizing the fact that the energy release rate is given identically by the J - integral, deLorenzi [B-3, B-4] has developed a method for calculating energy release rate rather simply. What is more, the increment in crack size divides out of his equations so that the results do not depend on the magnitude of this quantity at all. This method will be called the "deLorenzi method".

Before the filleted rods were analyzed, both the displacement substitution method and the deLorenzi method were used to analyze semicircular surface flaws of $a/d = 1/12$ in nonfilleted rods, the results being compared with each other and with results of other investigators [B-5, B-6] to assess the accuracy of the two methods. This comparison is displayed in Figure B-3. In the figure the SIF distributions around the crack front are displayed in non-dimensional form as geometry factors, F . The angle, θ , is measured from the tangent to the rod surface where it

intersects the origin of the semicircular flaw radius, as shown in Figure B-1. Two finite element meshes are compared, one using 102 elements and the other 204 elements. The various curves fall in a band which has a width of approximately 5% of the mean value. The mean value corresponds well with the analytical solution of a semicircular surface flaw in a semi-infinite body [B-6] and also with the results of [B-5]. The lower edge of the band is the curve corresponding to the 102 element mesh, deLorenzi method results, while the upper edge is the curve from [B-5]. If one takes the curves from [B-5, B-6] as essentially correct and if one bears in mind the fact that the results in [B-5] were obtained using the deLorenzi method with a 340 element mesh, then it is seen that as the mesh is refined when using the deLorenzi method the solution converges toward the correct one. This is not the case using the displacement substitution method. Moreover, the displacement substitution results oscillate in the region near the rod surface. Consequently, it is concluded that the deLorenzi method is the more reliable one. Also shown in Figure B-3 are curves for a rod with a fillet of $r/d = 1/4$ as determined using the deLorenzi method. It is clear that the 104 element and 208 element curves have the same relative locations as for the nonfilleted rod. In view of this it was decided that for the various filleted rod analyses the results obtained using the 102 element grid and the deLorenzi method could be considered to be approximately 5% low but otherwise correct. Although the results obtained using the displacement substitution method are included in

this appendix, because of their oscillatory nature it is thought that the results obtained with the deLorenzi method are more reliable. Therefore, it is recommended that for analysis purposes one use the curves reported as determined by the deLorenzi method and multiply them by 1.05.

Four different flaw sizes, $a/d = 1/6, 1/8, 1/12, 1/20$, were investigated along with three different fillet sizes, $r/d = 1/4, 1/7, 1/10$, as well as the nonfilleted rod condition, $r/d = 0$. It is generally thought that the stress intensity factors for surface flaws of size $a/d < 1/10$ can well approximate solutions for flaws in semi-infinite bodies, and the results given in Figure B-3 from references [B-5] and [B-6] support this. Figures B-4 and B-5 show the results determined in this study for nonfilleted rods, and they support this conclusion also except for the curves corresponding to $a/d = 1/20$. The curves for the other flaw sizes appear to be converging to some lower bound curve, possibly that of $a/d = 1/12$, but the $a/d = 1/20$ curve is far below this. It is felt that this curve is incorrect, but the reason has not been determined at this time.

Figures B-6 through B-9 are the results determined for the filleted rods using the deLorenzi method. The displacement substitution method counterparts are given in Figures B-10 through B-13. In each of these it is seen that the SIF values where the flaws intersect the fillet surfaces are much higher than for the nonfilleted rods, but not by an amount equivalent to the stress concentration factor for each particular fillet. Furthermore, it is seen that at the deepest penetrations of the flaws into the rods the SIF values are much lower, and, in fact, for fillet sizes approximately equal to or less than the flaw sizes the SIF's are actually smaller than those in nonfilleted rods. At first this seems a surprising result, but after some consideration it becomes clear why this is so and

why the values near the surfaces are lower than simply the nonfilleted rod values multiplied by the appropriate stress concentration factors.

An explanation of this behavior is best given after first recalling that the stress intensity factors of a flaw in a body loaded remotely by some stress distribution, σ_0 , are exactly the same as those obtained if one instead loads the flaw surface with tractions equal to the negative of those caused in an unflawed body by σ_0 . Specifically, one could obtain the SIF values of the unfilleted rods by applying a uniform pressure distribution on the flaw surfaces just as well as by applying a remote uniform tension, since in unflawed, nonfilleted rods the remote loading is transmitted undisturbed throughout the rods. Thus, one can consider that the SIF results given in Figure B-3, obtained in any way by anyone, are for flaws loaded on their surfaces by uniform pressures equal to the stress in $K_I = \frac{2}{\pi} \sigma_0 \sqrt{\pi a}$. This is illustrated in Figure B-14a. Similarly, if one wished to determine SIF values for flaws which occur at the roots of fillets in rods loaded in remote tension, one could do so by applying the negative of the stress distribution caused by that tension at the flaw location. In this case, however, the distribution would not be uniform, as is shown in Figure B-14b. It would have a maximum value at the fillet surface (equal to the stress concentration factor times the references stress) and would decrease at locations closer to the center of the rod. Comparing Figures B-14a,b it is clear that to simply multiply the SIF distributions for nonfilleted rods by the stress concentration factor would be to apply too much load on the surface and obtain considerable over-estimates. On the other hand if one uses the value of stress at the deepest penetration of the flaw one is using too little stress; however, in

some instances the value of the SIF at that location is predicted fairly well anyway.

This is also a surprising result at first glance, but is understandable if one recalls (see, for example, Broek [B-7], pages 78-80) that the stress near the location on the crack front where the SIF is being determined has more effect than stress at some distance from that location. So although the stress increases at locations closer to the rod surface, the effect on the SIF at the deepest penetration decreases, and the result is very similar to that of a uniform stress of the smallest magnitude acting on the flaw. For fillet sizes approximately equal to or less than the flaw sizes the value of stress at this location is less than the remotely applied tension, so the SIF is less than would occur in the nonfilleted rod. Likewise, the highest stress values have the most effect on the SIF near the surface and the lower stress values have less effect. The curves for filleted rods in Figures B-6 through B-9 and B-10 through B-13 demonstrate these facts very clearly, so they are not surprising after all.

Figures B-15 through B-17 and B-18 through B-20 illustrate the same results as in Figures B-6 through B-9 and B-10 through B-13 but grouped by fillet size rather than flaw size. Grouping them in this way shows clearly that the geometry factors decrease with increasing flaw size. This is due to the fact that the smaller the flaw size the more the concentrated stress at the surface affects its SIF distribution. Again, note that the $a/d = 1/20$ results are questionable, but the others are considered to be reliable.

The stress intensity factor distribution results presented in this appendix are useful for calculating SIF's for a few combinations of semicircular surface flaws occurring in filleted rods and for those

geometries which can be obtained by interpolation of these. More significantly, however, they illustrate the importance of the stress distribution in the region where the flaw is located. In order to determine SIF values for flaws in regions of stress concentration, then, it is best to determine the stress distribution in that region without a flaw and then use that distribution as the applied loading on the flaw surface. If a Green's function can be determined for the flaw geometry of interest, then any distribution of loading on the flaw surface can be handled with relatively little expense. Such functions have been determined for only a limited number of surface flaw conditions to date, however, so this method of SIF determination for surface flaws is not currently available for routine utilization. The Schwartz alternating method was demonstrated to be useful in determining SIF's for elliptical surface flaws by Shah and Kobayashi [B-8], and it has since been refined for such flaws by Vijayakumar and Atluri [B-9] and Nishioka and Atluri [B-10]. In view of the results shown in this report, it should be particularly powerful for elliptical surface flaws occurring in regions of stress concentration since it utilizes an analytical solution for a buried elliptical flaw subject to arbitrary loading on its surfaces along with a finite element solution of the actual geometry without a flaw. In order to improve fatigue crack growth analysis capabilities a relatively inexpensive method for determining SIF values for surface flaws of arbitrary shape located in regions of arbitrary stress distribution needs to be devised, and it is recommended that this be pursued in future research efforts.

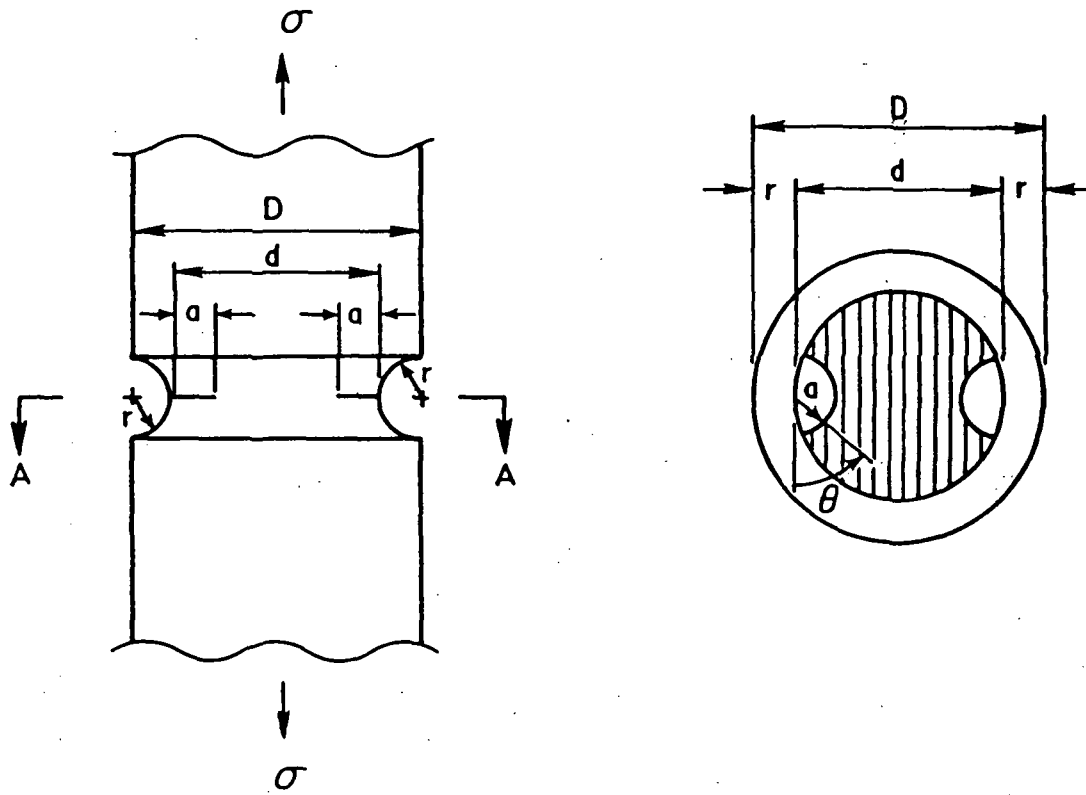


Figure B-1: Filleted Rod and Flaw Geometry

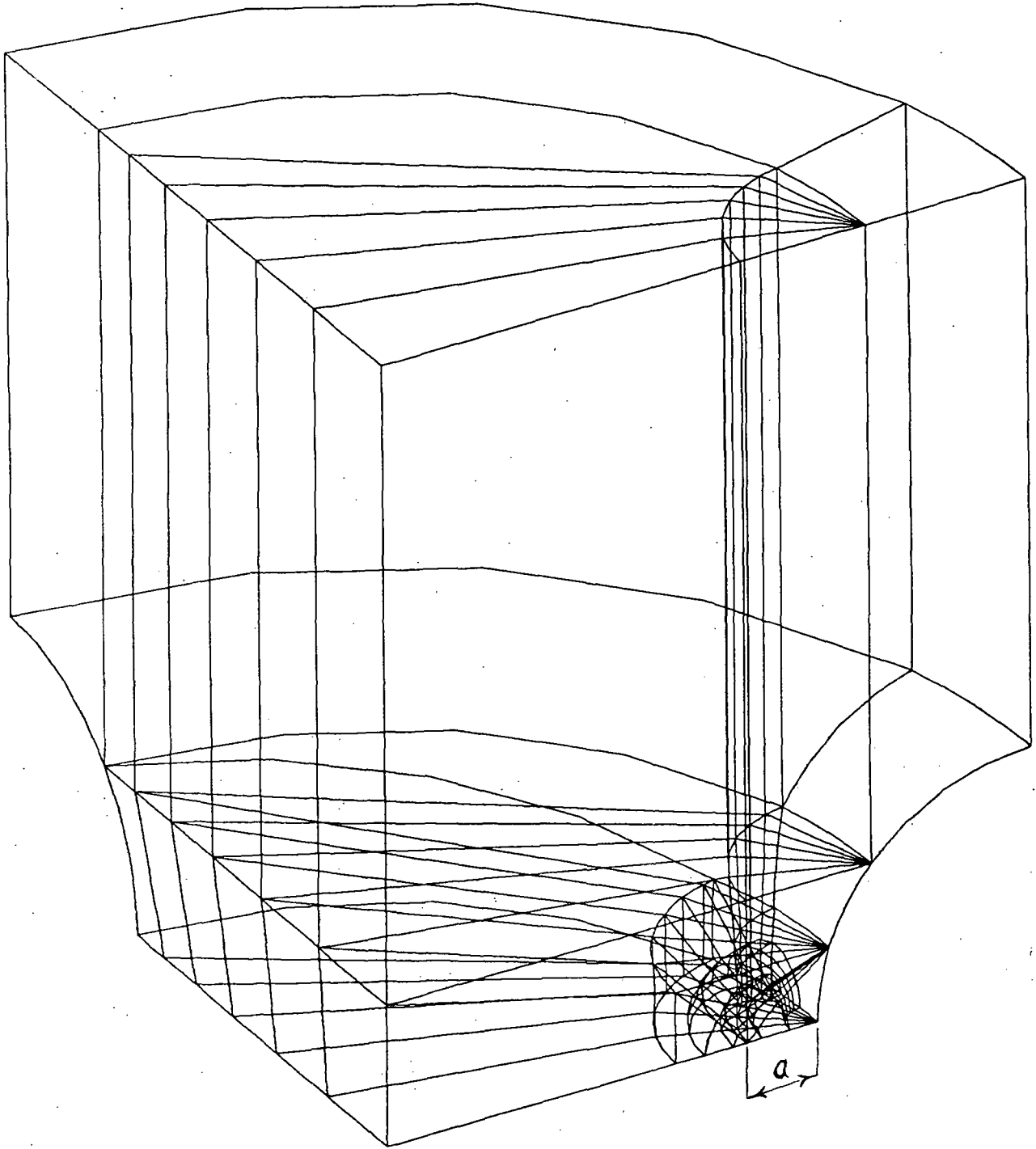


Figure B-2. Typical Finite Element Mesh for a Filleted Rod Flaw Analysis

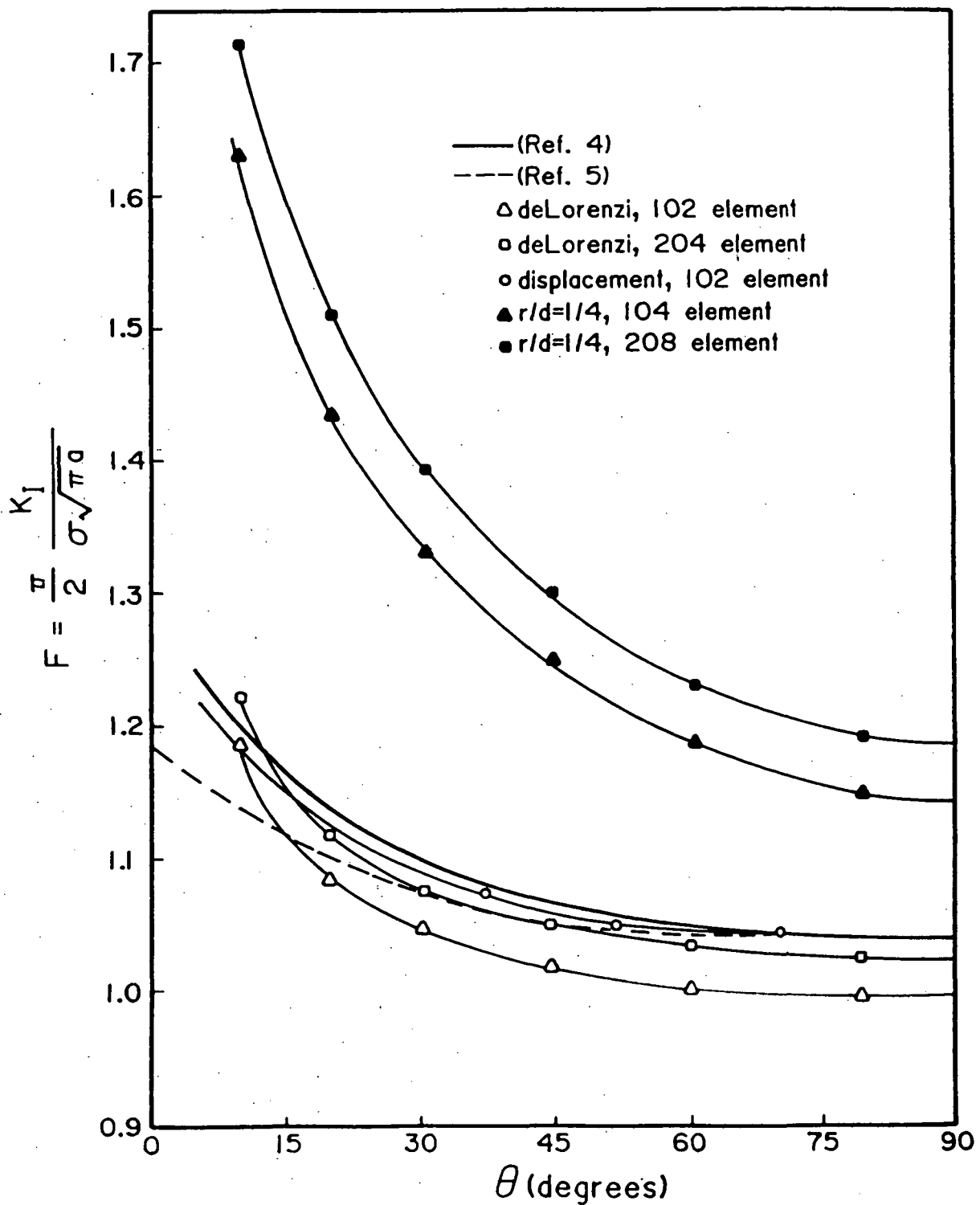


Figure B-3. Analysis Comparisons

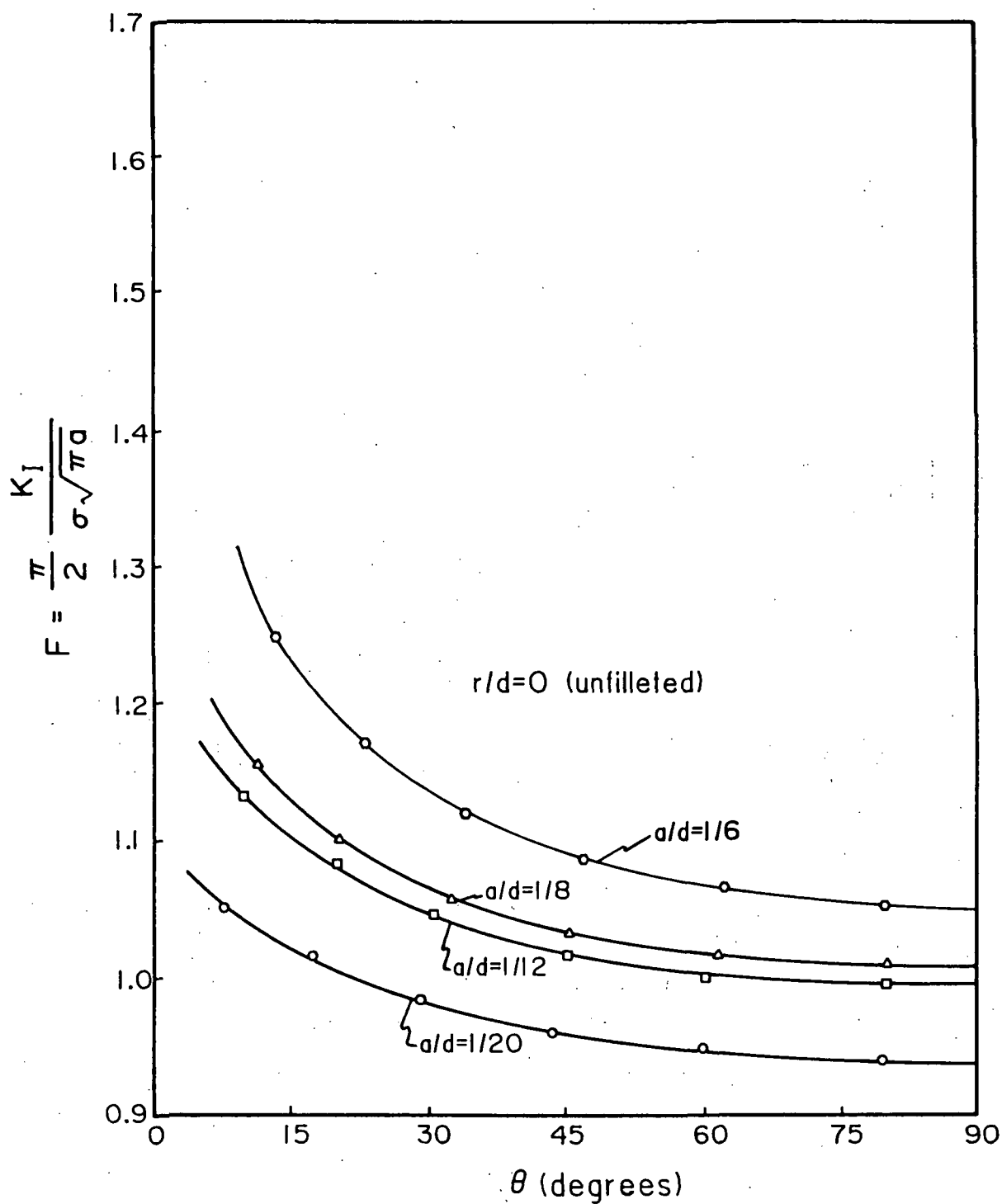


Figure B-4. Geometry Factor for Nonfilleted Rod by de Lorenzi Method.

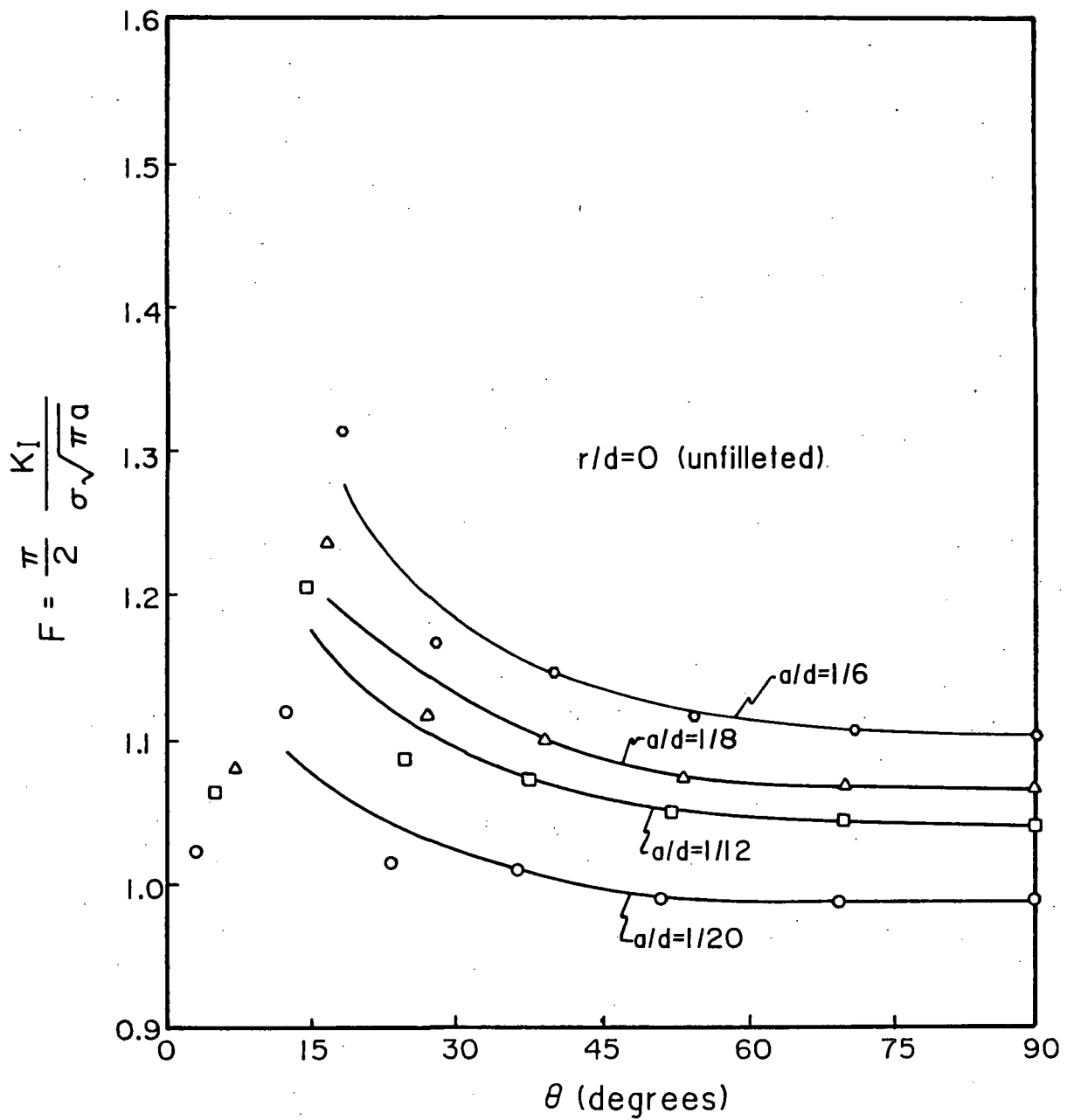


Figure B-5. Geometry Factor for Nonfilleted Rod by Displacement Substitution Method

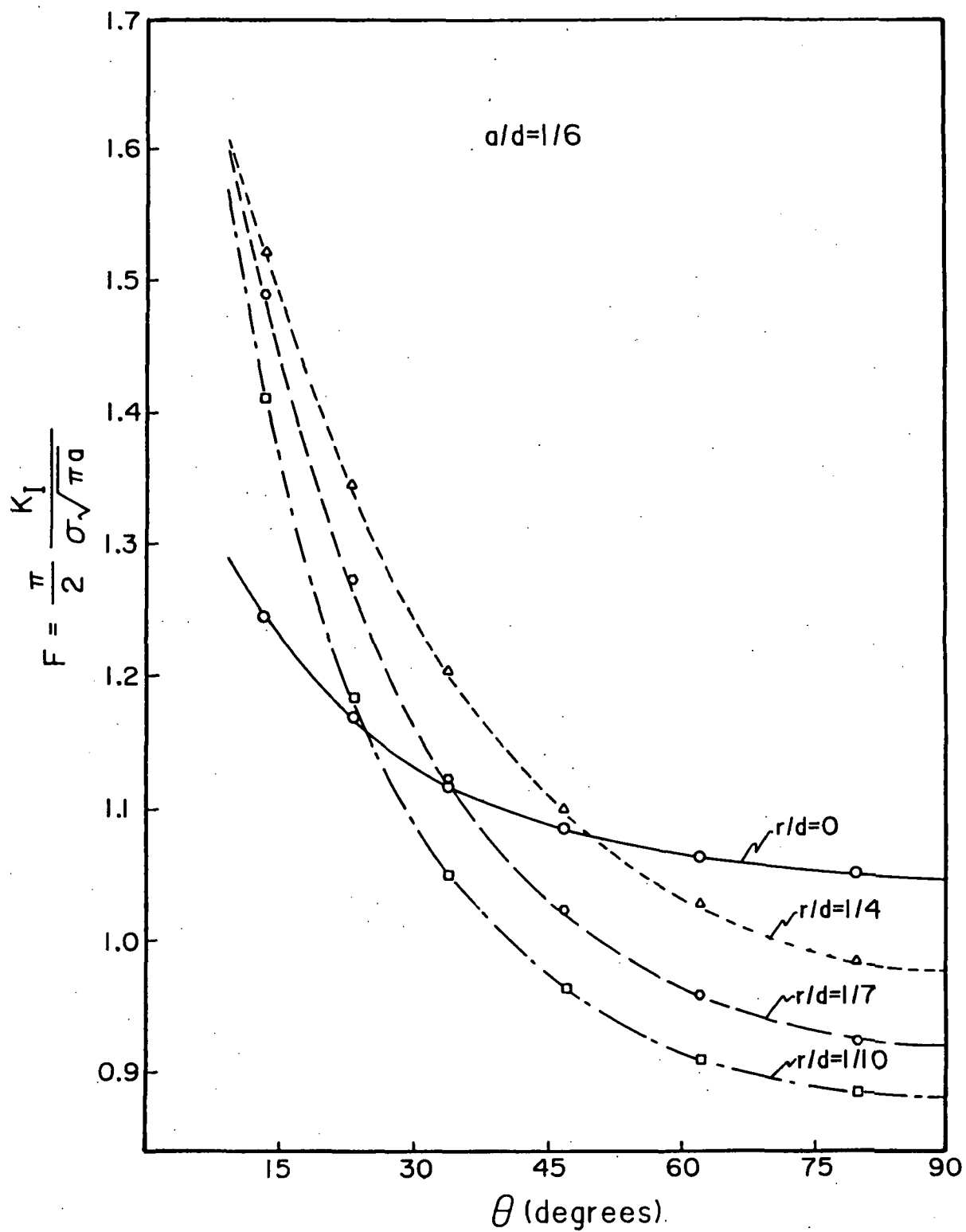


Figure B-6. Geometry Factor for $a/d = 1/6$ Flaw by de Lorenzi Method

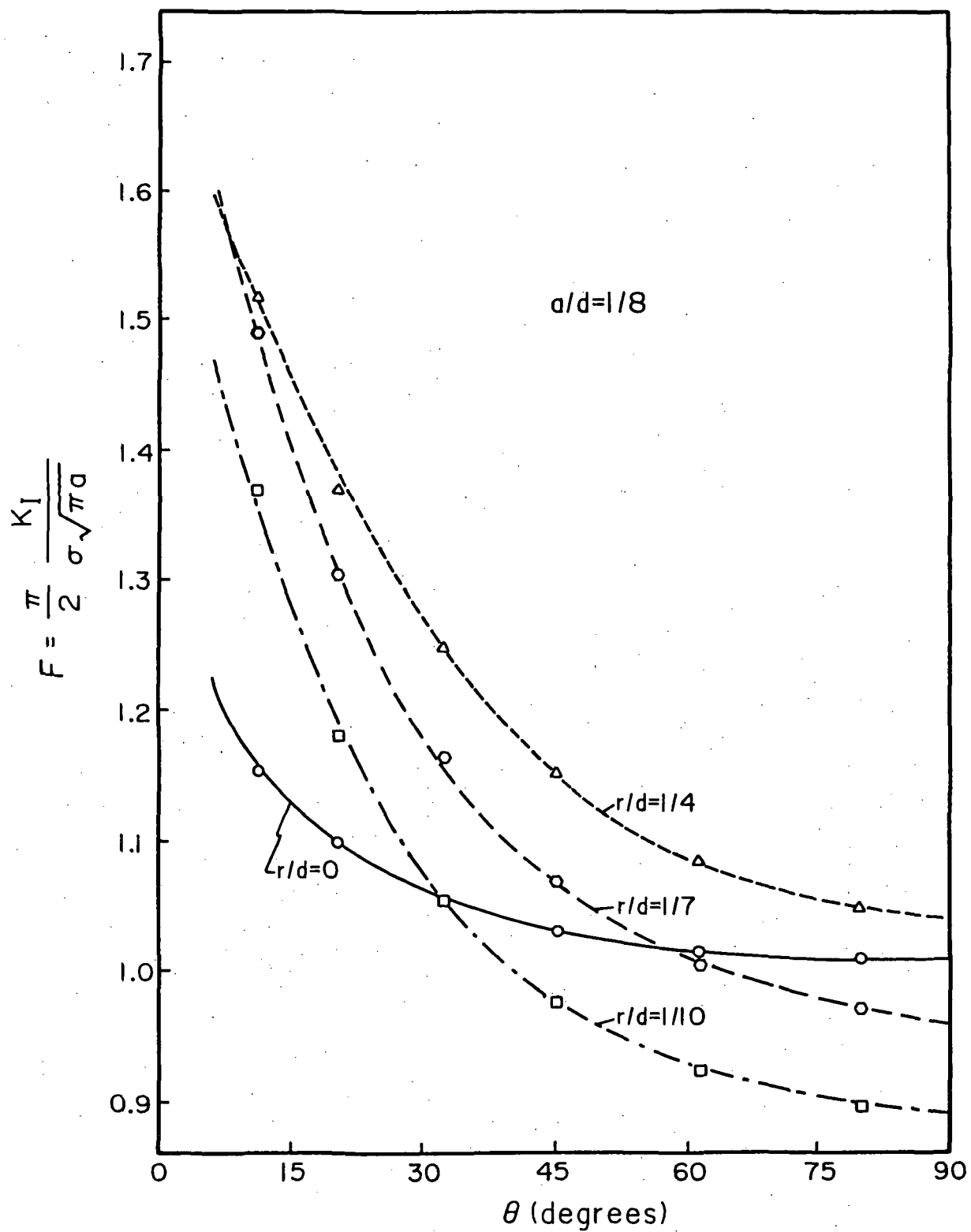


Figure B-7. Geometry Factor for $a/d = 1/8$ Flaw by de Lorenzi Method

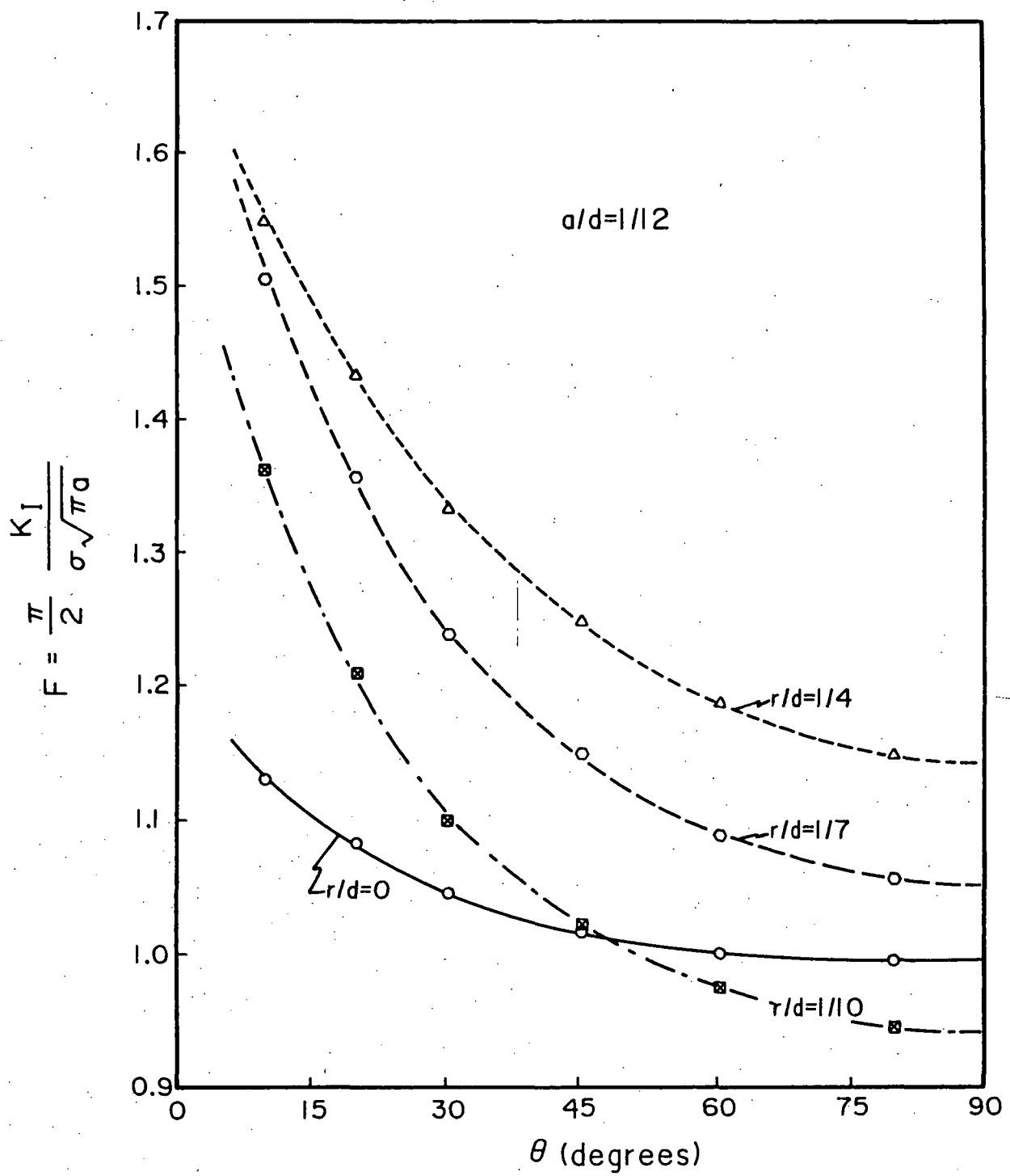


Figure B-8. Geometry Factor for $a/d = 1/12$ Flaw by de Lorenzi Method

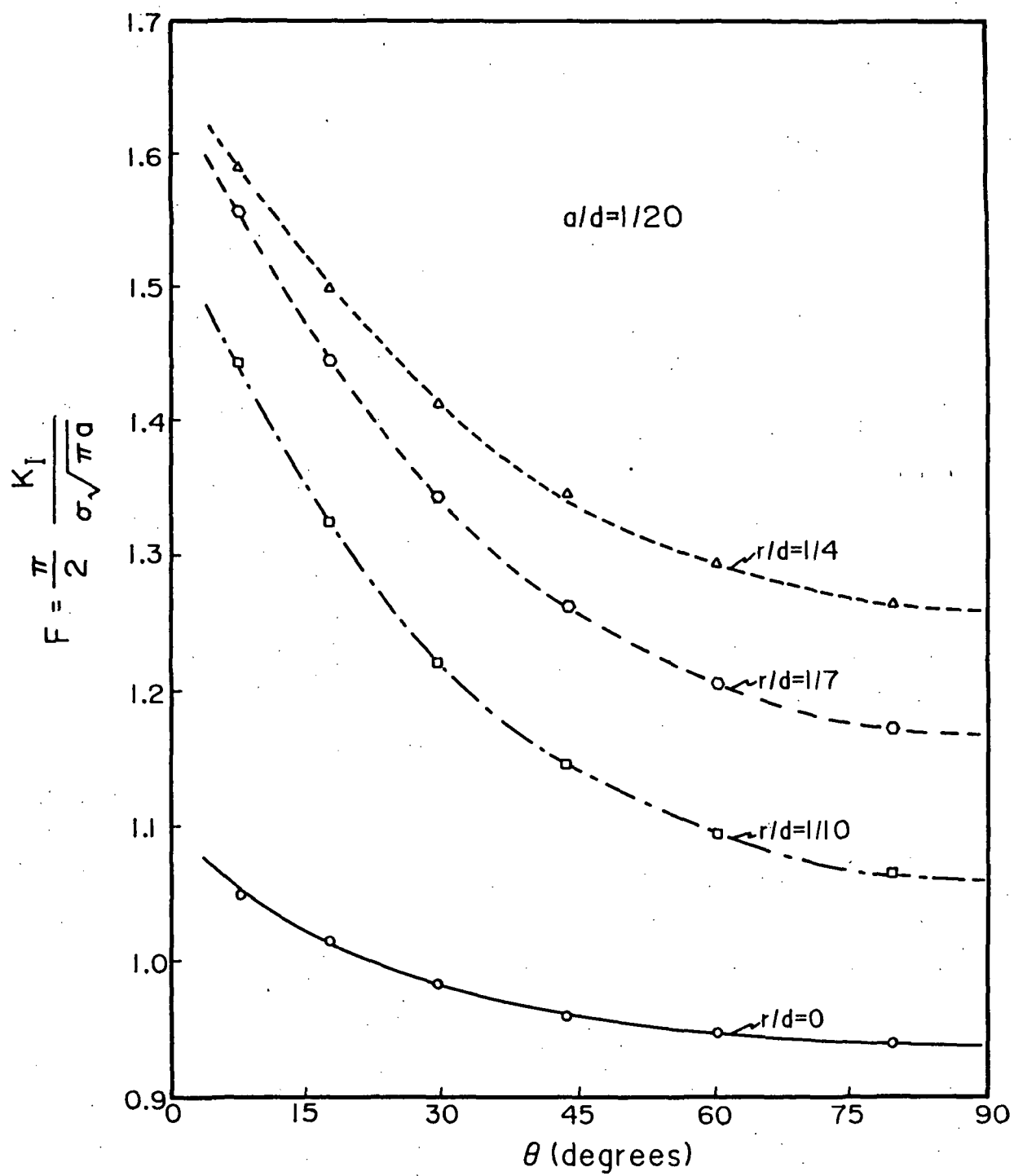


Figure B-9. Geometry Factor for $a/d = 1/20$ Flaw by de Lorenzi Method

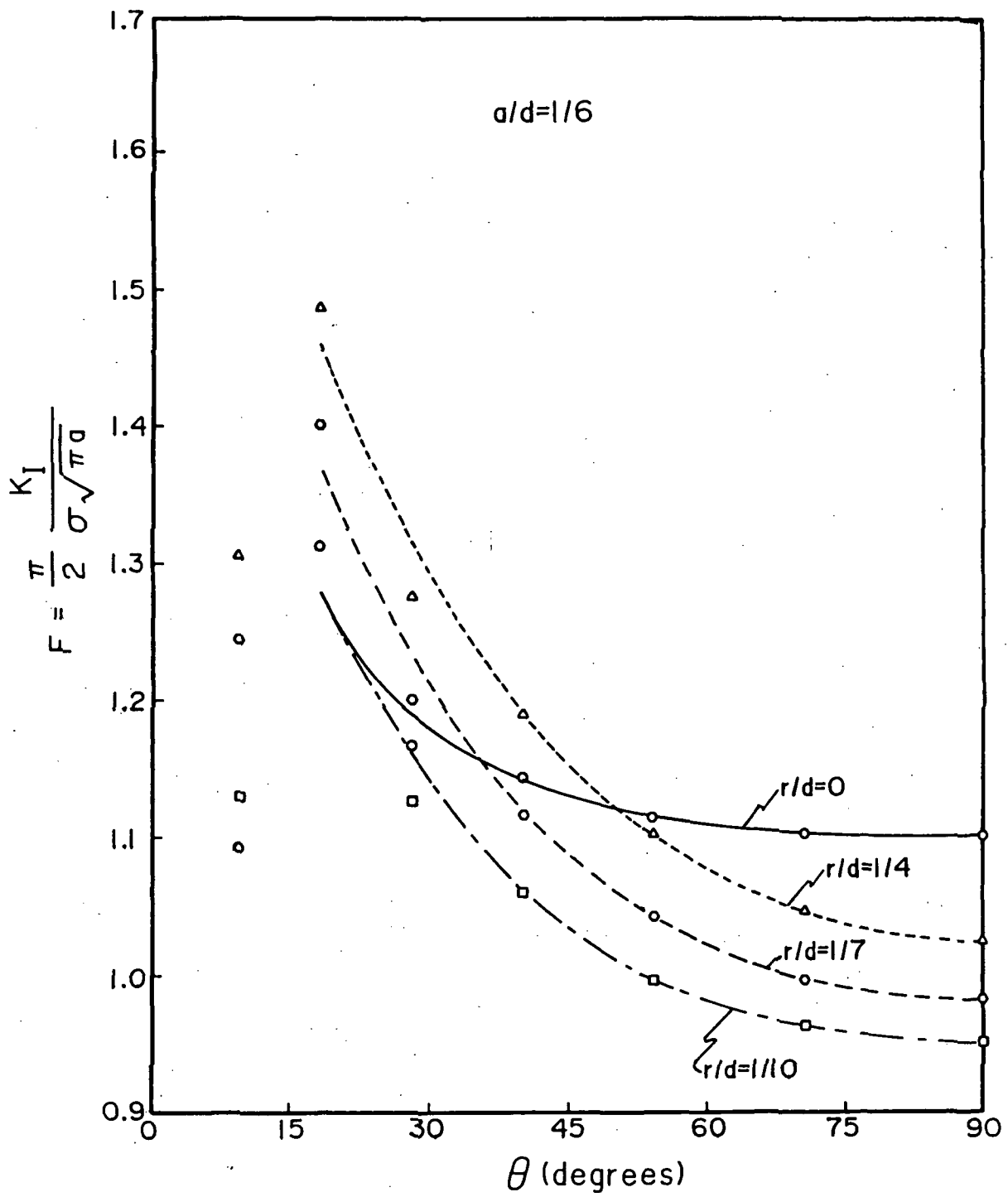


Figure B-10. Geometry Factor for $a/d = 1/6$ Flaw by Displacement Substitution Method

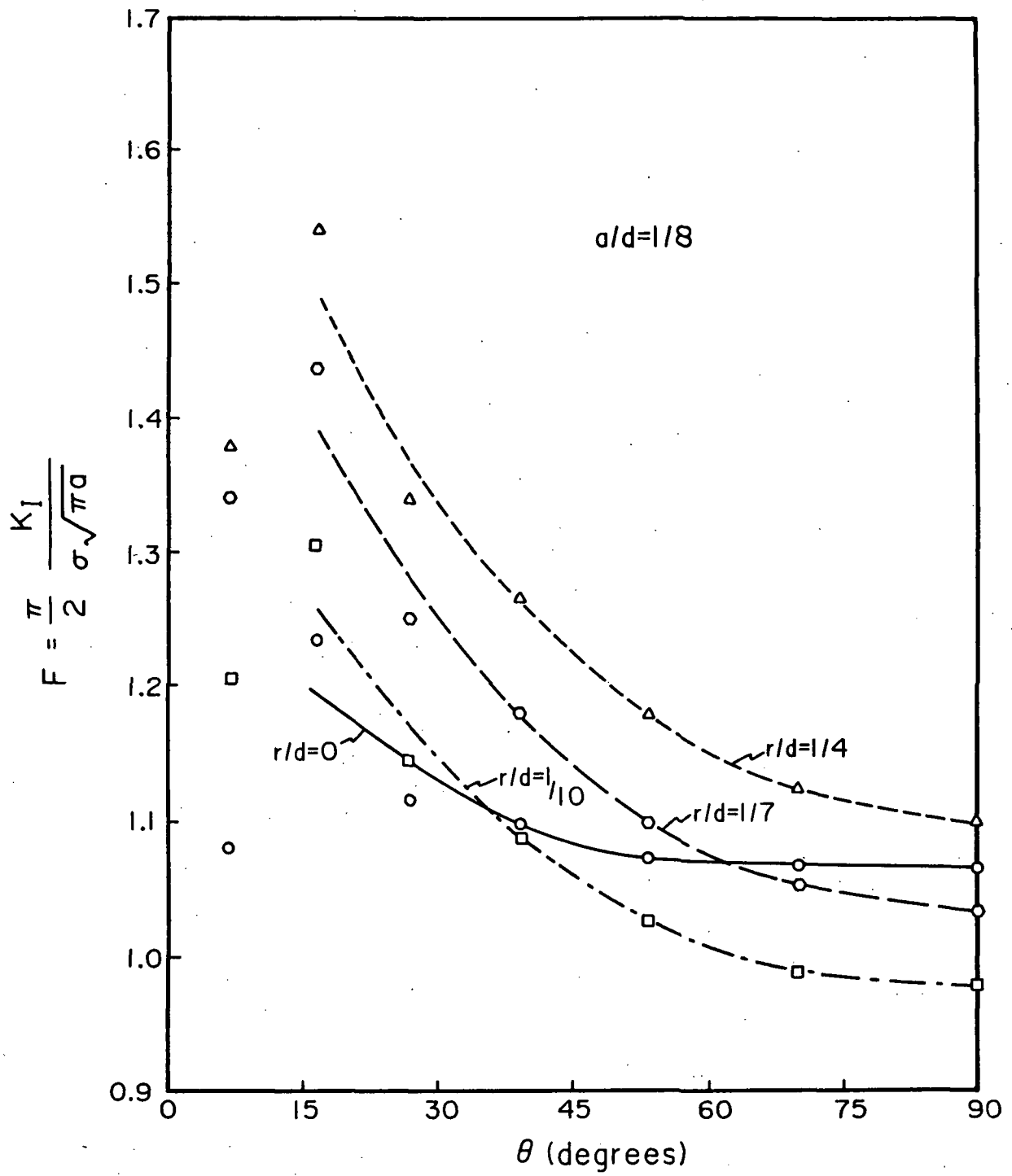


Figure B-11. Geometry Factor for $a/d = 1/8$ Flaw by Displacement Substitution Method

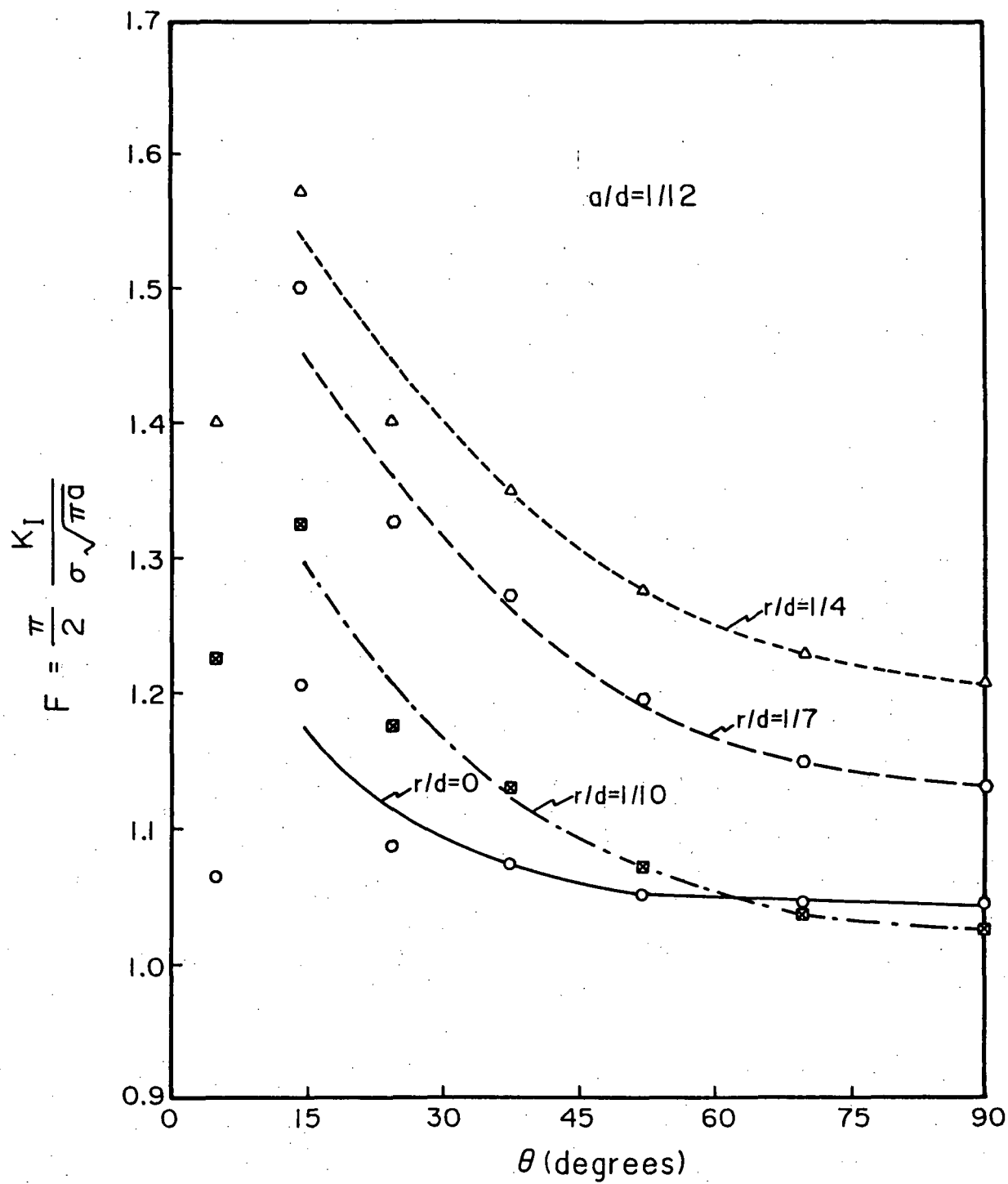


Figure B-12. Geometry Factor for $a/d = 1/12$ Flaw by Displacement Substitution Method

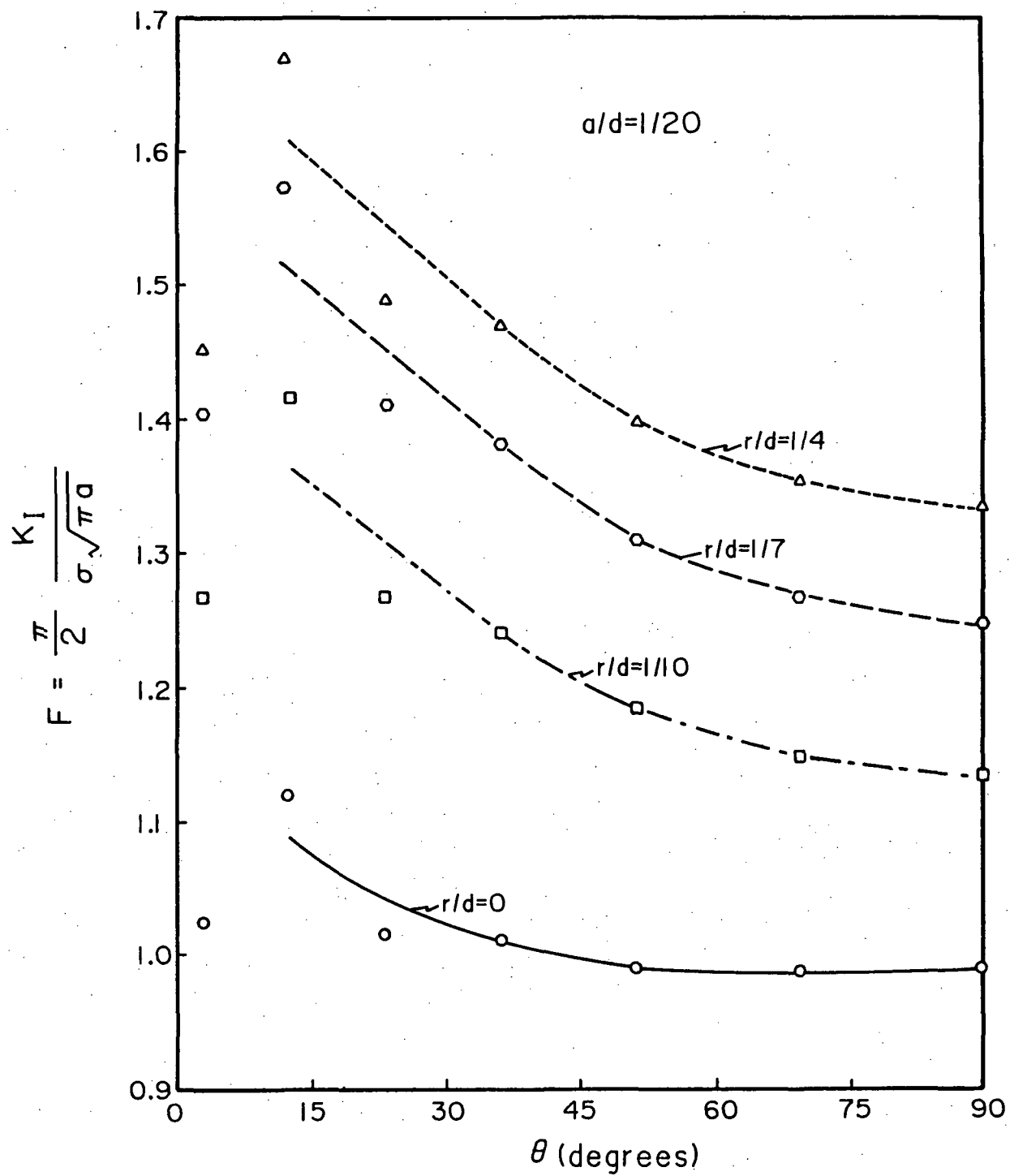
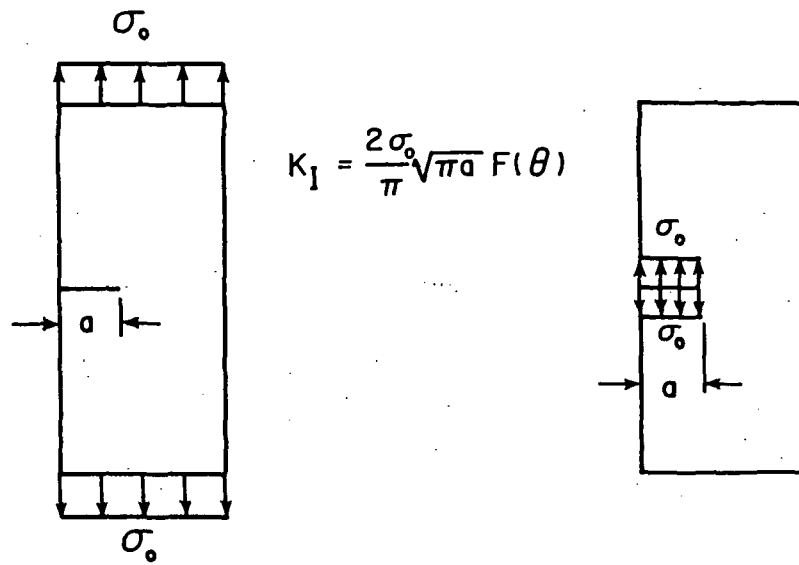
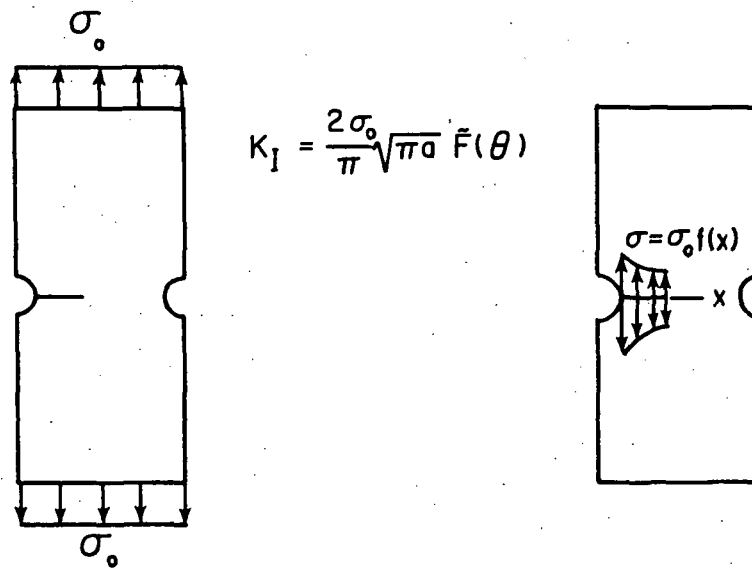


Figure B-13. Geometry Factor for $a/d = 1/20$ Flaw by Displacement Substitution Method



(a)



(b)

Figure B-14. Stress Distributions at Flaw Locations in (a) Nonfilleted Rods and (b) Filleted Rods

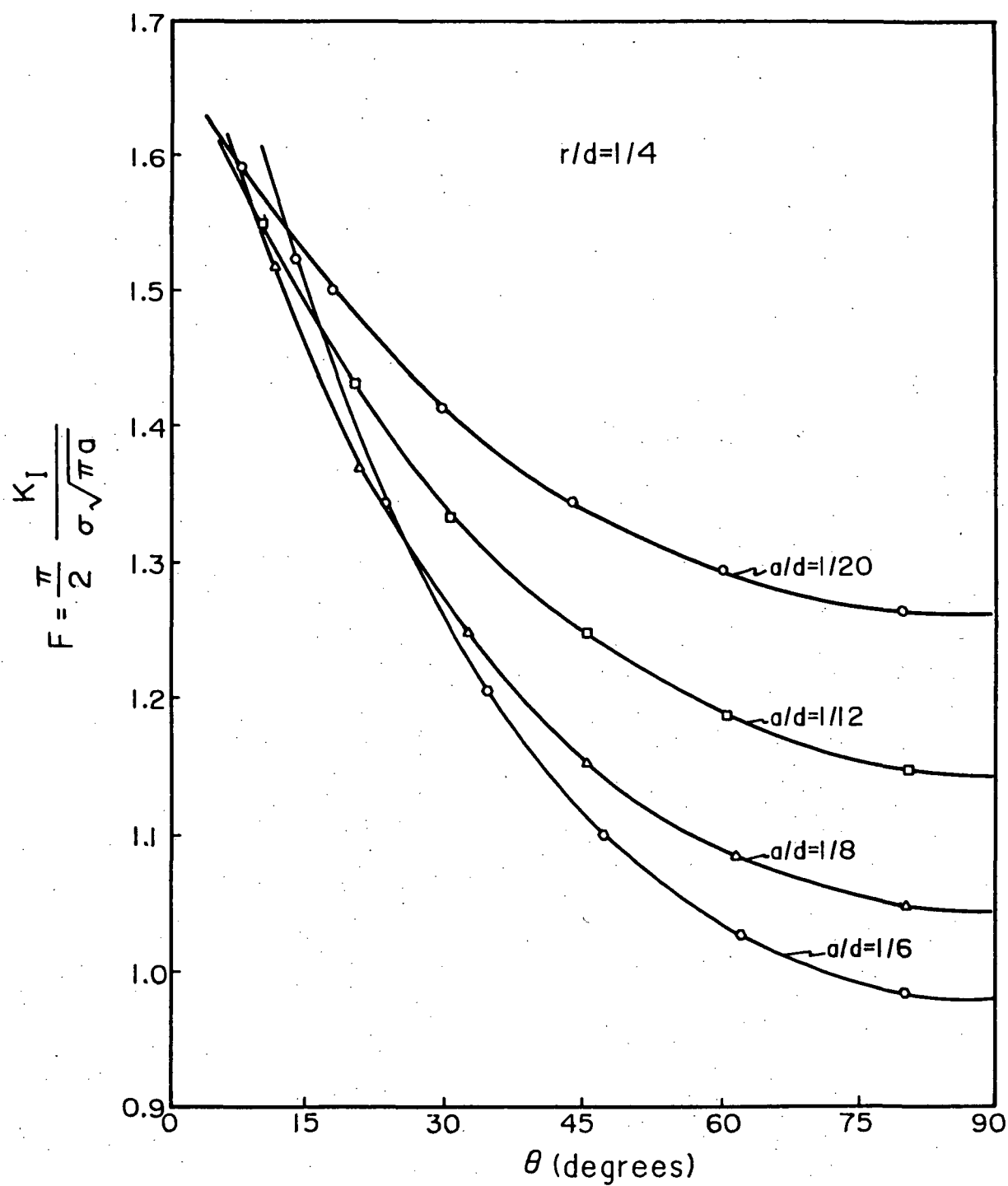


Figure B-15. Geometry Factor for $r/d = 1/4$ Filleted Rod by de Lorenzi Method

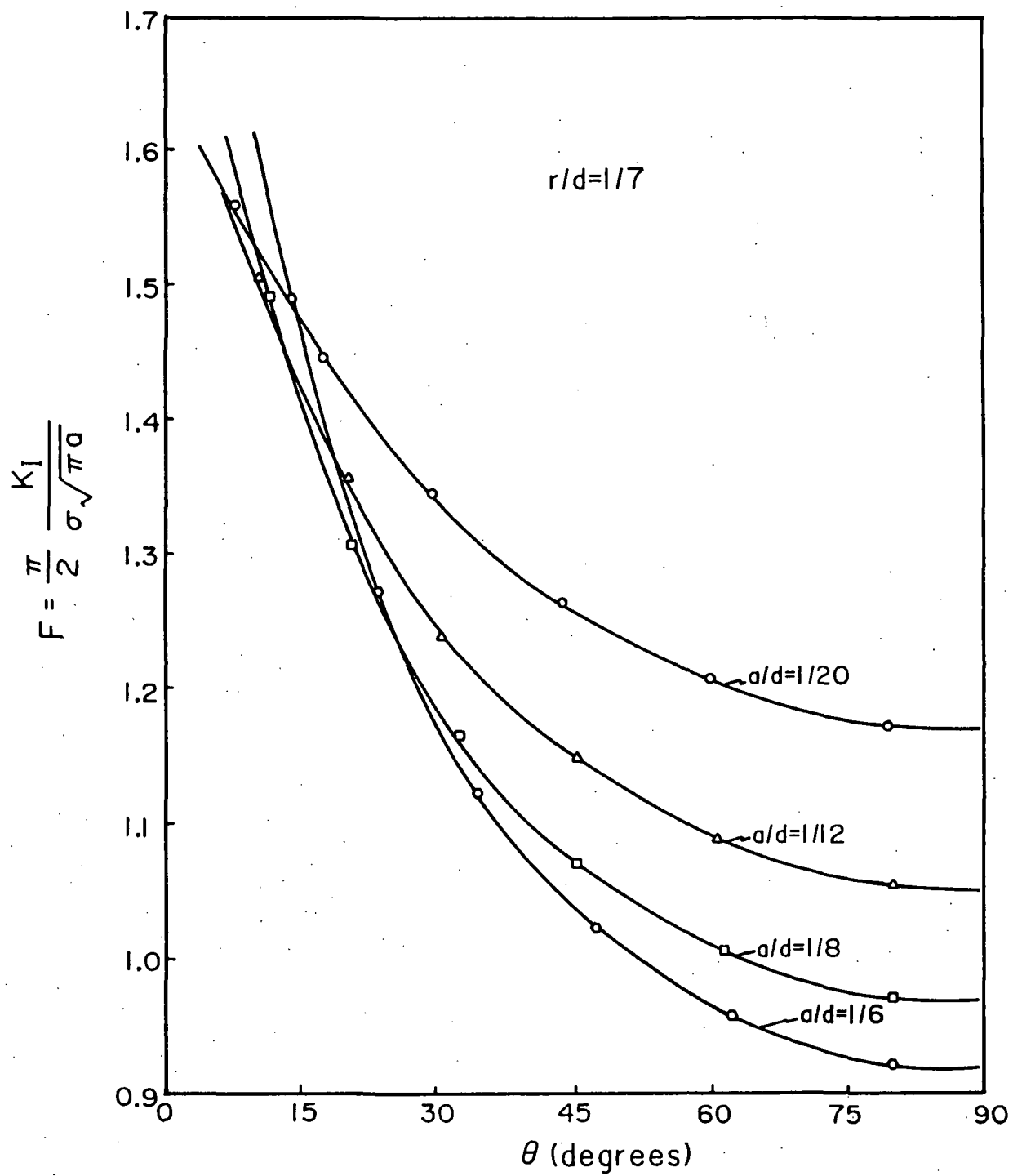


Figure B-16. Geometry Factor for $r/d = 1/7$ Filleted Rod by de Lorenzi Method

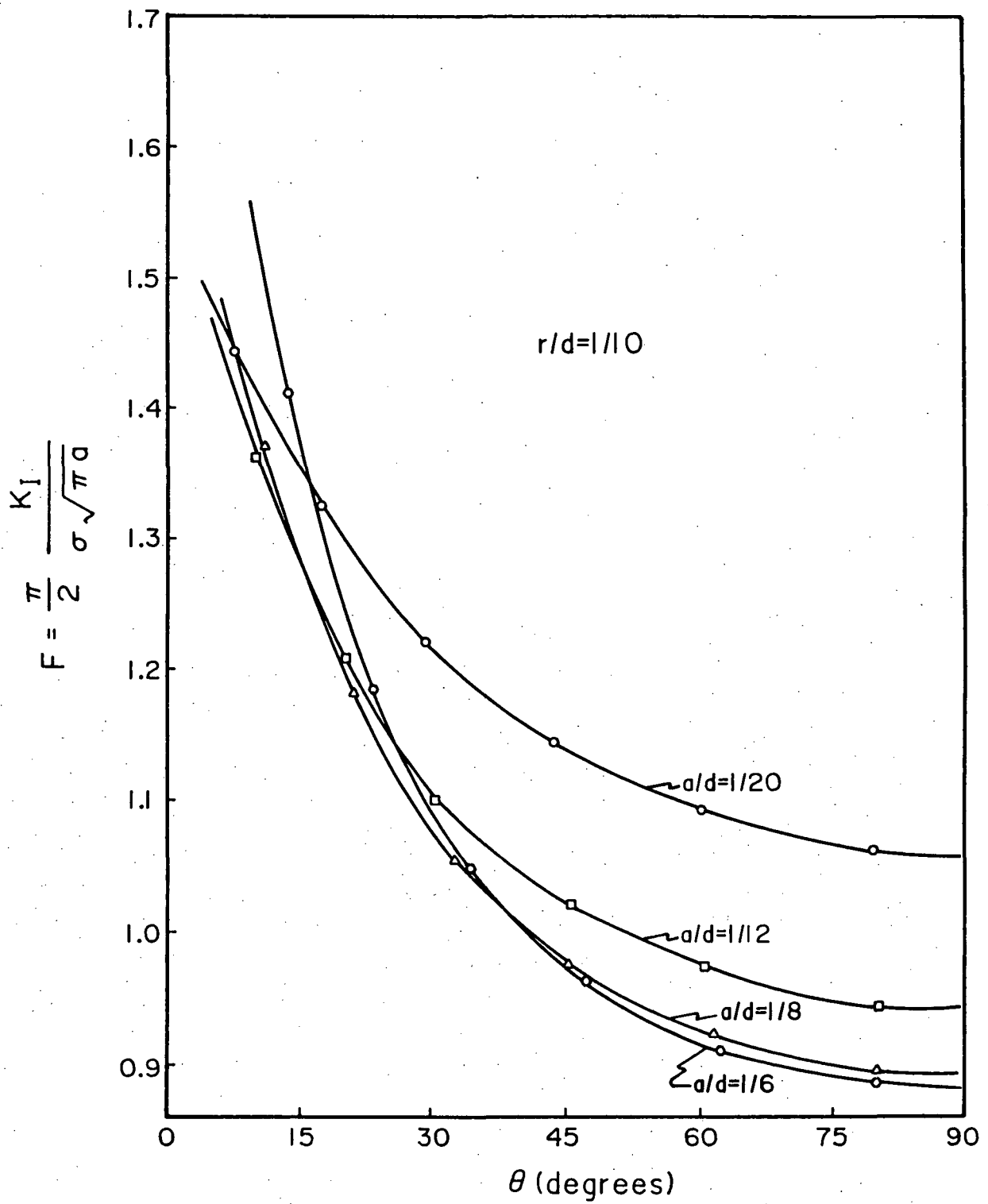


Figure B-17. Geometry Factor for $r/d = 1/10$ Filleted Rod by de Lorenzi Method

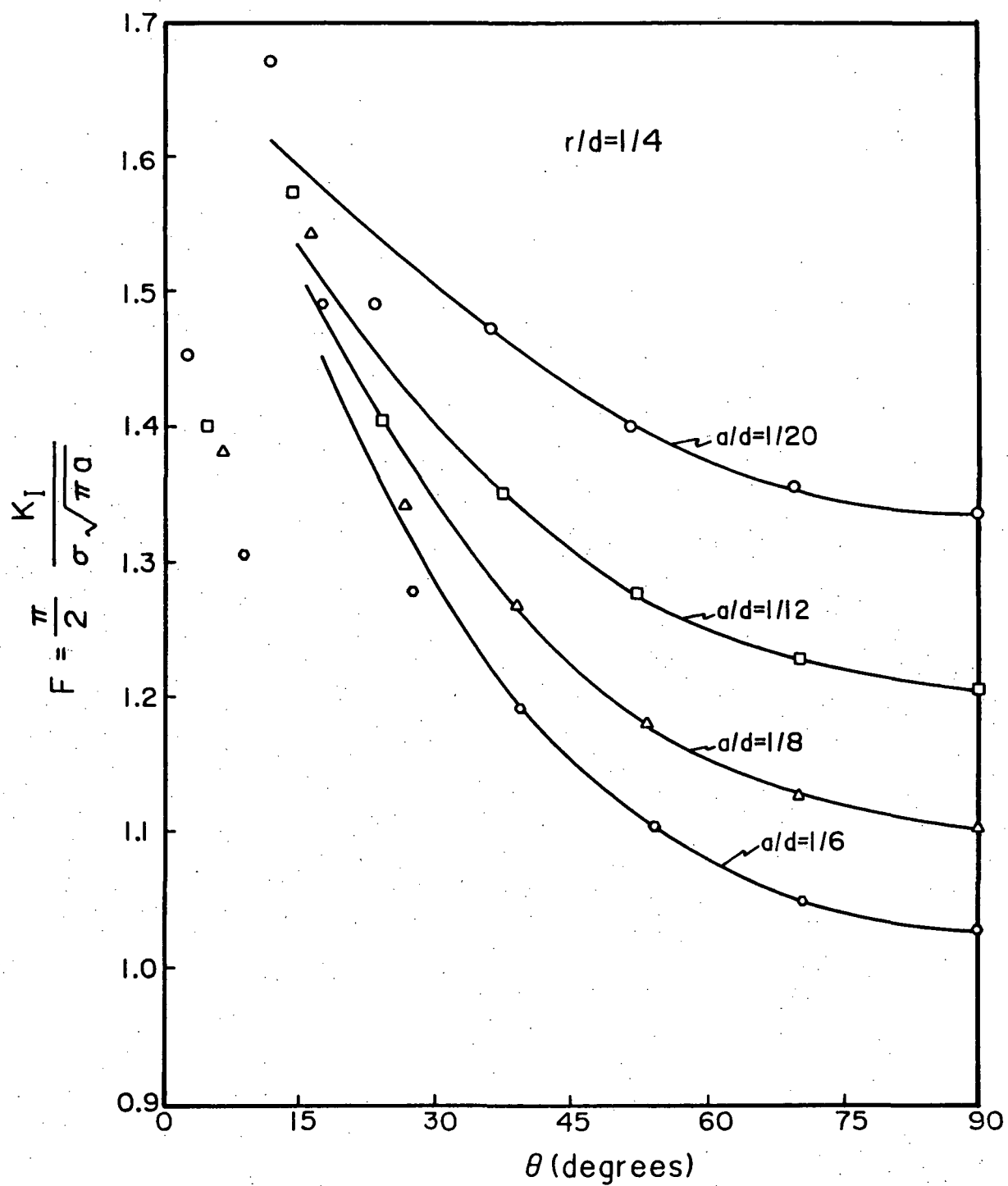


Figure B-18. Geometry Factor for $r/d = 1/4$ Filleted Rod by Displacement Substitution Method

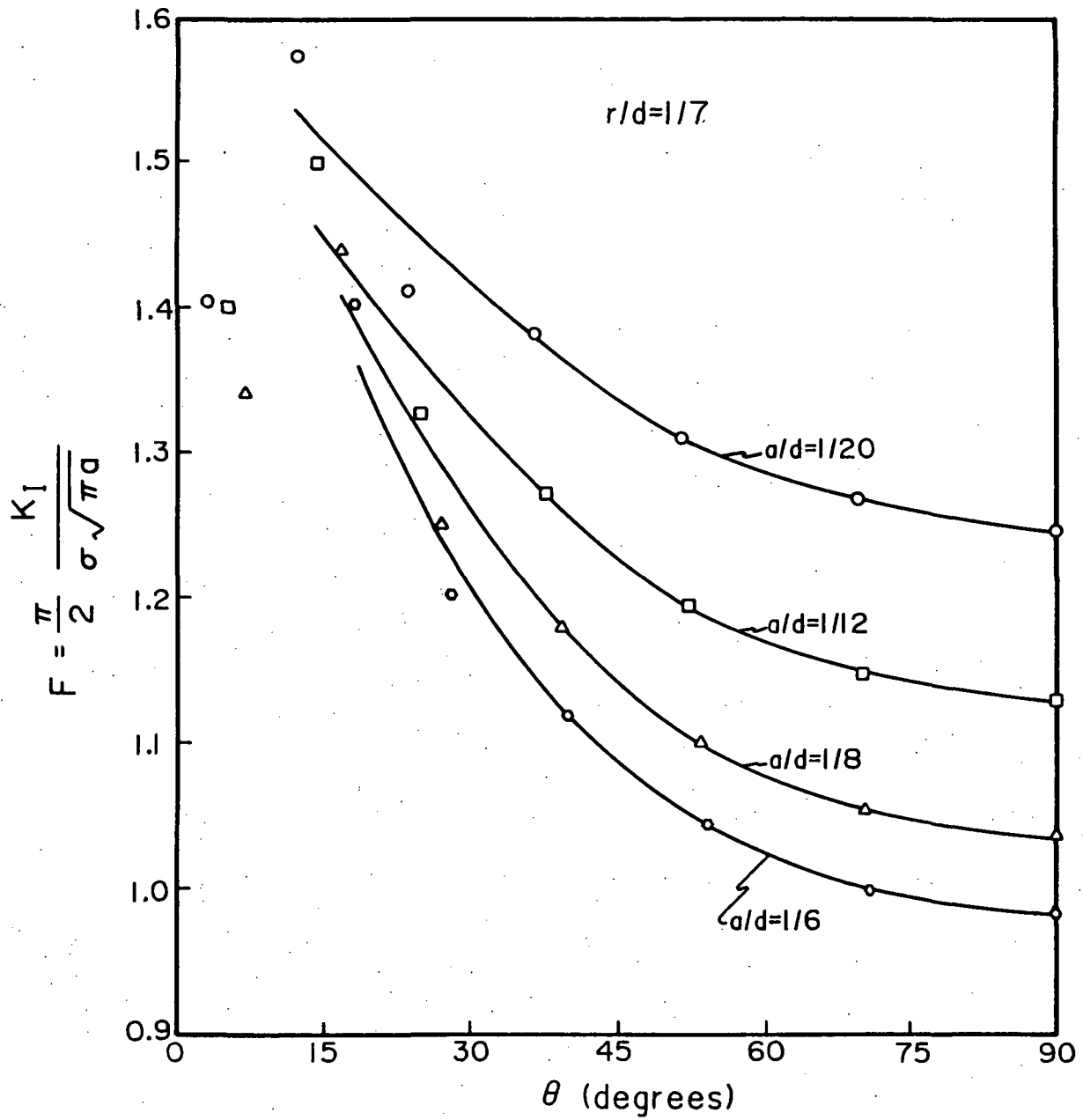


Figure B-19. Geometry Factor for $r/d = 1/7$ Filleted Rod by Displacement Substitution Method

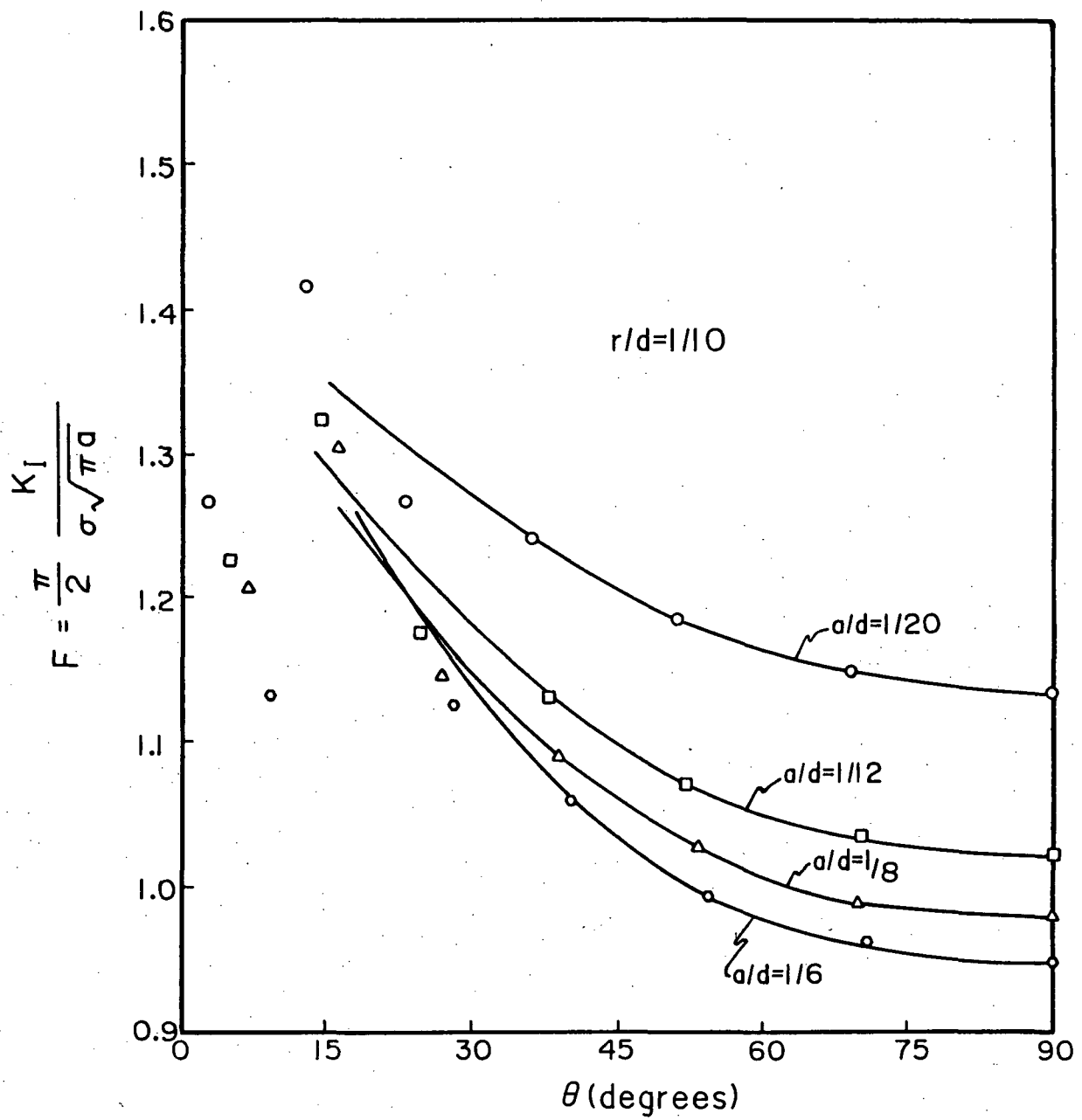


Figure B-20. Geometry Factor for $r/d = 1/10$ Filleted Rod by Displacement Substitution Method

References for Appendix B

- [B-1] Nord, K., Three-Dimensional Fracture Analysis by Quadratic Isoparametric Finite Elements, M.S.E. thesis, The University of Alabama in Huntsville, May 1983.
- [B-2] Barsoum, R. S., "Triangular Quarter-Point Elements as Elastic and Perfectly-Plastic Crack Tip Elements," Int. J. Num. Meth. Eng., II, 1977, pp. 85-98.
- [B-3] deLorenzi, H. G., "On the Energy Release Rate and the J-Integral for 3-D Crack Configurations," Int. J. Frac., 19, 1982, pp. 183-193.
- [B-4] deLorenzi, H. G., "Energy Release Rate Calculations by the Finite Element Method," Eng. Frac. Mech., 21, 1985, pp. 129-143.
- [B-5] Trantina, G. G., H. G. deLorenzi and W. W. Wilkening, "Three-Dimensional Elastic-Plastic Finite Element Analysis of Small Surface Cracks," Eng. Frac. Mech., 18, 1983, pp. 925-938.
- [B-6] Tada, H., P. C. Paris and G. R. Irwin, The Stress Analysis of Cracks Handbook, Del Research Corporation, St. Louis, Missouri, 1985.
- [B-7] Broek, D., Elementary Engineering Fracture Mechanics, 3rd edition, Martinus Nijhoff, 1982.
- [B-8] Shah, R. C. and A. S. Kobayashi, "On the Surface Flaw Problem," The Surface Crack: Physical Problems and Computational Solutions, edited by J. L. Swedlow, ASME, 1972, pp. 79-124.
- [B-9] Vijayakumar, K. and S. N. Atluri, "An Embedded Elliptical Flaw in an Infinite Solid, Subject to Arbitrary Crack Face Traction," J. Appl. Mech., 48, 1981, pp. 88-96.
- [B-10] Nishioka, T. and S. N. Atluri, "Analytical Solution for Embedded Elliptical Cracks, and Finite Element Alternating Method for Elliptical Surface Cracks, Subjected to Arbitrary Loadings," Eng. Frac. Mech., 17, 1983, pp. 247-268.